

# Regularising Inverse Problems with Generative Machine Learning Models

M A G Duff<sup>1</sup>, N D F Campbell<sup>2</sup> and M J Ehrhardt<sup>1</sup>

<sup>1</sup> Department of Mathematics, University of Bath, Bath, BA2 7AY, UK

<sup>2</sup> Department of Computer Science, University of Bath, Bath, BA2 7AY, UK

E-mail: M.A.G.Duff@bath.ac.uk

## Abstract.

Deep neural network approaches to inverse imaging problems have produced impressive results in the last few years. In this paper, we consider the use of generative models in a variational regularisation approach to inverse problems. The considered regularisers penalise images that are far from the range of a generative model that has learned to produce images similar to a training dataset. We name this family *generative regularisers*. The success of generative regularisers depends on the quality of the generative model and so we propose a set of desired criteria to assess models and guide future research. In our numerical experiments, we evaluate three common generative models, autoencoders, variational autoencoders and generative adversarial networks, against our desired criteria. We also test three different generative regularisers on the inverse problems of deblurring, deconvolution, and tomography. We show that the success of solutions restricted to lie exactly in the range of the generator is highly dependent on the ability of the generative model but that allowing small deviations from the range of the generator produces more consistent results.

*Keywords* inverse problems, generative models, machine learning, imaging

Submitted to: *Inverse Problems*

## 1. Introduction

Solving an inverse problem is the process of calculating an unknown quantity,  $x \in \mathcal{X}$ , from observed, potentially noisy, measurements,  $y \in \mathcal{Y}$ . In this work  $\mathcal{X}$  and  $\mathcal{Y}$  are assumed to be real finite-dimensional vector spaces. The two are related by a forward model,  $A : \mathcal{X} \rightarrow \mathcal{Y}$ , which, for simplicity, is assumed to be linear, giving the equation

$$Ax = y. \tag{1}$$

Inverse problems are nearly always ill-posed: there does not exist a unique solution or small deviations in the data lead to large deviations in the solution. Addressing this ill-posedness is critical in applications where decision making is based on the recovered solutions. Throughout this paper, we focus on image reconstruction problems, where  $x \in \mathcal{X}$  is an image, but there are many other applications.

Generally, ill-posed problems are solved by incorporating some prior information often given in the form of a regulariser in a variational regularisation framework [82, 44, 14]. Consider the optimisation problem

$$x^* \in \arg \min_x L_y(Ax) + \lambda R(x), \tag{2}$$

where  $L_y : \mathcal{Y} \rightarrow \mathbb{R} \cup \{\infty\}$  is a similarity measure; the constant  $\lambda$  is a regularisation parameter and  $R : \mathcal{X} \rightarrow \mathbb{R} \cup \{\infty\}$  is the regularisation function that is small when some desired Property of the image is fulfilled. For example, *Tikhonov* regularisation, encourages the reconstruction to be small in the 2-norm and Total Variation (*TV*) regularisation [79] allows large gradients (e.g. edges) to occur sparsely in the reconstruction. These hand-built regularisers, although very successful, are better suited to some types of images over others, e.g. TV is best suited to cartoon-like images. A natural question to ask is that, given a set of images, what regularisation function would work well?

There is a wide range of research into learning regularisation functions. Examples include sparse coding and dictionary learning [6] where a sparse basis for feasible solutions is learned. Others have considered regularisation by a learned denoiser [90, 60, 77], penalising images that differ from their denoised version. More recently, ‘adversarial regularisation’ [57] considers regularisation by a neural network trained to discriminate between desired images and undesired images which contain artefacts. In work called Network Tikhonov (NETT) [55], Li et al. consider regularisation by a general neural network. They are able to analyse the properties of the neural network required to deal with the ill-posedness of the problem. Alberti et al. [7] consider learning the parameters of a Tikhonov type regulariser and prove theoretical results comparing learned and optimal regularisation schemes. For a recent overview on approaches to using deep learning to solve inverse problems, see for example [11].

Here we consider the case that the prior information can be provided by a learned generative model. The assumption is that the plausible reconstructions exhibit local regularities, global symmetries or repeating patterns and so naturally lie on some lower dimensional manifold, a subset of  $\mathcal{X}$ . A *generator*  $G : \mathcal{Z} \rightarrow \mathcal{X}$  takes points from a *latent*

space,  $\mathcal{Z}$ , where  $\dim(\mathcal{Z}) \ll \dim(\mathcal{X})$ , parameterising this lower dimensional manifold. The generator is taken to be a parameterised function, for example a neural network, trained such that the generated points  $G(z) \in \mathcal{X}$  are similar to some pre-defined training set.

In this work, we consider regularisation functionals,  $R_G$ , that penalise values of  $x \in \mathcal{X}$  that are far from the range of the generator  $G$ , and call these *generative regularisers*. We contribute a brief existing approaches to generative regularisers including [17, 28, 37, 88]. A popular example [17] limits solutions to those that are exactly in the range of the generator thus giving

$$x^* = G(z^*), \quad z^* \in \arg \min_z \|AG(z) - y\|_2^2 + \lambda \|z\|_2^2. \quad (3)$$

Generative regularisers are both flexible and interpretable. The machine learning element is independent of the forward model and the noise type and samples from the trained generator can demonstrate the priors placed on the solution. By mixing a data-driven approach with more traditional variational regularisation, it is anticipated to gain the best of both worlds, utilising the advancements in model-based inverse problems over the last century while the learned aspect will provide more specific information than a hand crafted regulariser. In this work, we test different generative regularisers, inspired by the literature, on convolution, compressed sensing and tomography inverse problems, including on a knee MRI dataset.

The success of a generative regularisers will depend on the quality of the generator. Having clear success criteria is vital in inverse problems where the applications, for example in medicine, can be critical. We propose a set of criteria that would be beneficial for a generative model destined for use in a generative model, and demonstrate possible methods of testing generative models against this criteria.

The paper is laid out as followed: Section 2 gives a mathematical introduction to autoencoders (AEs), variational autoencoders (VAEs) and generative adversarial networks (GANs); Section 3 groups together existing approaches for generative regularisers; Section 4 describes a set of desirable properties for a generator, specifically for use in inverse problem and demonstrates so potential methods of evaluating generative models against the proposed criteria; and Section 5 provides numerical experiments testing generative regularisers on inverse problems. Conclusions and future work is set out in the last section, Section 6.

### 1.1. Mathematical Notation

Define the *image space*  $\mathcal{X}$ , *measurement space*  $\mathcal{Y}$  and *latent space*  $\mathcal{Z}$ , which are each Euclidean. Throughout we use the  $p$ -norm, for  $p \geq 1$  and  $x \in \mathcal{X}$ ,  $\|x\|_p := (\sum_i |x_i|^p)^{1/p}$ .

Take,  $G_\theta : \mathcal{Z} \rightarrow \mathcal{X}$  to be a *generator*, a parameterised function, usually a neural network. The parameter is dropped when the meaning is obvious. Define the *range* of the generator,  $G$ , as  $Range(G) = \{x \in \mathcal{X} \mid \exists z \in \mathcal{Z} \text{ s.t. } G(z) = x\}$ .

Throughout,  $P$  is a *probability distribution* and  $p$  is a *probability density*. Define the *expectation* of a function  $f$  on space  $\mathcal{A}$  with respect to distribution  $P$  as  $\mathbb{E}_{x \sim P} f(x) =$

$\int_{\mathcal{A}} f(x)dP(x)$ . For corresponding density,  $p$ ,  $\mathbb{E}_{x \sim P} f(x) = \int_{\mathcal{A}} f(x)p(x)dx$ .

Define  $P_Z$  to be a *prior distribution on the latent space*. Let  $P^*$  be the distribution of desired solutions to the inverse problem. The training and testing set for the generative model and ground truth testing set for the inverse problem are assumed to be samples from this distribution. Define the testing set  $\mathcal{X}_{\text{Test}} = \{x_1, \dots, x_M\} \subset \mathcal{X}$ .

The characteristic function, defined for an arbitrary set  $\mathcal{C}$  is defined as

$$\iota_{\mathcal{C}}(t) = \begin{cases} 0 & \text{for } t \in \mathcal{C} \\ \infty & \text{for } t \notin \mathcal{C} \end{cases}.$$

## 2. Generative Models

This Section provides background on generators and generative models, focusing in particular on three approaches: autoencoders (AEs), variational autoencoders (VAEs) and generative adversarial networks (GANs).

### 2.1. Autoencoder (AE)

An autoencoder (AE) has two parts, an encoder and a decoder. The encoder encodes an image in some latent space and the decoder takes a point in this latent space and decodes it, outputting an image. The lower dimensional latent space forms a ‘bottleneck’ that forces the network to learn representations of the input with a reduced dimensionality and preventing the model from simply learning the identity mapping.

Denote the encoder  $E_{\psi} : \mathcal{X} \rightarrow \mathcal{Z}$  and the decoder  $G_{\theta} : \mathcal{Z} \rightarrow \mathcal{X}$ . Assume the encoder and decoder are neural networks with parameters  $\psi$  and  $\theta$ , respectively. The networks are trained by minimizing a reconstruction loss

$$\mathcal{J}(\psi, \theta) = \mathbb{E}_{x \sim P^*} \|x - G_{\theta}(E_{\psi}(x))\|_2^2, \quad (4)$$

with respect to  $\theta$  and  $\psi$ . Post training, the decoder can be used as a generator, taking values in  $\mathcal{Z}$  and outputting points in  $\mathcal{X}$ , as set out in the introduction, Section 1.

The encoder is not required to cover a certain area of a latent space, or indeed restricted to a certain area, thus generating from points in the latent space may not lead to outputs similar to the training set. Furthermore, close points in the latent space may not lead to similar generated images. Nevertheless, this method of training is simple and has recently been used in learned singular valued decomposition and for applications in sparse view CT [15, 68].

### 2.2. Probabilistic Models

In order to add greater structure and meaning to the latent space and to discourage unrealistic outputs from the generator we take a probabilistic approach. We consider a prior distribution,  $P_Z$ , and push it through the generator,  $G$  to give a generated distribution  $P_G$  on  $\mathcal{X}$ . Sampling from the prior and then applying the generator allows

samples to be taken from  $P_G$ . The generator,  $G$ , is chosen to minimise the distance between  $P_G$  and  $P^*$ ,

$$d(P^*, P_G). \quad (5)$$

We define the pair  $(P_Z, G)$  to be a *generative model*.

### 2.3. Generative Adversarial Network (GAN)

The choice of Wasserstein distance in (5) leads to the Wasserstein GAN [9], a popular generative model. Following the derivation given in Appendix A, the task of minimising the Wasserstein distance becomes

$$\min_{\theta} \max_{\phi} \{ \mathcal{L}(\theta, \phi) := \mathbb{E}_{x \sim P^*} D_{\phi}(x) - \mathbb{E}_{z \sim P_Z} D_{\phi}(G_{\theta}(z)) \}. \quad (6)$$

The *generator*  $G_{\theta} : \mathcal{Z} \rightarrow \mathcal{X}$  is as before, and we have introduced a *discriminator*  $D_{\phi} : \mathcal{X} \rightarrow \mathbb{R}$  which must be 1-Lipschitz. To enforce the Lipschitz constraint a penalty term,  $\mathbb{E}_{x \sim \hat{P}} (\|\nabla D_{\phi}(x)\|_2 - 1)^2$ , is added to the loss function of the discriminator. Samples of  $\hat{P}$  are calculated as  $\hat{x} = tG_{\theta}(z) + (1-t)x$  for  $t \sim \mathcal{U}[0, 1]$ ,  $x \sim P^*$  and  $z \sim P_Z$  [36].

The objective in (6) is a saddle point problem. We say that  $(\theta^*, \phi^*)$  is a local saddle point if  $\mathcal{L}(\theta^*, \phi) \leq \mathcal{L}(\theta^*, \phi^*) \leq \mathcal{L}(\theta, \phi^*)$  for all  $\phi$  and  $\theta$  in neighbourhoods of  $\phi^*$  and  $\theta^*$ , respectively. The desired result,  $P_G = P^*$ , with  $D_{\phi} \equiv \text{constant}$ , is a saddle point, however, there are many other, non-optimal critical points.

In the game theoretic interpretation of (6) [33] a generative model competes with a discriminative model. The generator produces fake data and the discriminative model determines real from fake. The discriminator aims to accurately identify real images, maximising  $\mathbb{E}_{x \sim P^*} D_{\phi}(x)$ , and generated (fake) images, maximising  $-\mathbb{E}_{z \sim P_Z} D_{\phi}(G_{\theta}(z))$ . The generator tries to force the discriminator to label generated images as real, minimising  $-\mathbb{E}_{z \sim P_Z} D_{\phi}(G_{\theta}(z))$ .

*2.3.1. Other GAN Variations* Other choices of distance measure, in (5), may lead to other GAN variations. For example, choosing  $d$  in (5) to be an f-divergence leads to a range of GAN options [65]. Taking  $d$  to be the Jensen-Shannon Divergence gives the original, ‘vanilla’, GAN [33]

$$\mathcal{L}(\theta, \phi) = \mathbb{E}_{z \sim P_Z} [\log(1 - D_{\phi}(G_{\theta}(z)))] + \mathbb{E}_{\tilde{x} \sim P^*} [\log(D_{\phi}(\tilde{x}))]. \quad (7)$$

For definitions and details of the derivation see for example [92].

For the numerical results in this paper we choose to use a Wasserstein GAN (6) as it is often more robust to a range of network designs and there is less evidence of mode collapse, when the generator learns just part of the target distribution, compared to the ‘vanilla’ GAN [9].

#### 2.4. Variational Autoencoder (VAE)

For another choice of distance,  $d$ , in (5), take the Kullback–Leibler (KL) divergence. This choice leads to another common generative model, the variational autoencoder (VAE) [50].

Following the derivation in Appendix A, the objective can be written as a minimisation of

$$\mathcal{J}(\psi, \theta) = \mathbb{E}_{x \sim P^*} \left( \mathbb{E}_{z \sim \mathcal{N}_{x,\psi}} \left[ \frac{\|x - G_\theta(z)\|_2^2}{2\rho^2} \right] + d_{KL}(\mathcal{N}_{x,\psi} \| p_Z) \right). \quad (8)$$

where  $\mathcal{N}_{x,\psi} := \mathcal{N}(\mu_\psi(x), \text{diag}(\sigma_\psi^2(x)))$ ,  $d_{KL}$  is the KL divergence and  $\mu_\psi, \sigma_\psi^2 : \mathcal{X} \rightarrow \mathcal{Z}$  are *encoder mean* and *encoder variance*, neural networks with parameters  $\psi$ . The constant  $\rho$  is a hyperparameter chosen to reflect the ‘noise level’ in the training dataset.

We can interpret the two terms in (8) as a reconstruction term and a regularisation term, respectively. In the first term, the expected reconstruction and the original image is compared. Encoding to a distribution,  $\mathcal{N}_{x,\psi}$ , enforces that points close to each other in the latent space should produce similar images. In the second term, the KL divergence encourages the encoded distributions to be close to the prior,  $p_Z$ . The prior is usually taken to be the standard normal distribution and this also encourages independence between the latent dimensions. The balance between the two terms is determined by the noise level,  $\rho$ .

### 3. Overview of Generative Models used in Regularisers for Inverse Problems

In this Section, we consider three different generative regularisers for use in the variational regularisation objective (2), which are

$$R_G(x) = \min_{z \in \mathcal{Z}} \iota_{\{0\}}(G(z) - x) + R_z(z) \quad (9)$$

$$R_G(x) = \min_{z \in \mathcal{Z}} \|G(z) - x\|_2^2 + R_z(z) \quad (10)$$

$$R_G(x) = \min_{z \in \mathcal{Z}, u \in \mathcal{X}} \iota_{\{0\}}(G(z) + u - x) + R_z(z) + R_u(u). \quad (11)$$

Here  $R_z$  and  $R_u$  provide optional additional regularisation.

#### 3.1. Optimisation over the latent space

Regularisation of the form (9) restricts solutions to be in the range of the generator. Substituting this into (2) gives

$$x^* = G(z^*), \quad z^* \in \arg \min_{z \in \mathcal{Z}} L_y(AG(z)) + \lambda R_z(z). \quad (12)$$

This describes searching over the latent space for the encoding that best fits the data.

Bora et al. [17] first proposed this strategy, applying it to compressed sensing problems, where  $A \in \mathbb{R}^{\dim \mathcal{Y} \times \dim \mathcal{X}}$  is a measurement matrix taking  $\dim \mathcal{Y} < \dim \mathcal{X}$  linear measurements. Their choice  $R_z(z) = \|z\|_2^2$  reflects the Gaussian prior placed on the

latent space. There are a number of interesting applications using method (12), such as denoising [88], seismic waveform inversion [62], blind deconvolution [12] and phase retrieval [40].

Bora et al. [17] assume the existence of an optimisation scheme that can minimise (12) with small error and from this probabilistically bound the error between the result of the optimisation and the ground truth. However, the non-convexity introduced by the generator makes any theoretical guarantees on the optimisation extremely difficult. Hand and Voroninski [39] consider gradient-based optimisation. Assuming that  $A$  is a matrix with Gaussian entries, the network  $G$  has random Gaussian weights and the network is sufficiently expansive, then they prove that,  $z \mapsto \|AG(z) - y\|_2^2$  has a descent direction everywhere outside the minimiser and a negative multiple of the minimiser, with high probability.

### 3.2. A Constrained Optimisation Problem on the Range( $G$ )

An equivalent problem formulation to (12) is the constrained optimization problem

$$x^* \in \arg \min_{x \in \text{Range}(G)} L_y(Ax) + R_x(x), \quad (13)$$

where  $R_x$  gives the option for further regularisation of  $x$ . This formulation, by Shah and Hegde [83], is optimised by Projected Gradient Descent:

$$w_{t+1} = x_t - \eta A^T(Ax_t - y) \quad (14a)$$

$$z_{t+1} = \arg \min_z \|w_{t+1} - G(z)\|_2 \quad (14b)$$

$$x_{t+1} = G(z_{t+1}). \quad (14c)$$

With analogies to the restricted isometry Property in compressed sensing [20], the authors introduce the *Set Restricted Eigenvalue Condition*. If the set restricted eigenvalue condition holds then the operator,  $A$ , preserves the uniqueness of signals in the range of  $G$ . They prove that if  $A$  is a bounded random Gaussian matrix that satisfies the S-REC with some probability, then they can give a lower bound on the probability that the sequence  $x_t$ , defined by (14a) to (14c), converges to  $x^\dagger$ , where  $Ax^\dagger = y$ .

The projected gradient approach simply moves the problem of non-convex optimisation to (14b). Xu et al. [95] instead use a neural network trained to take values  $x \in \mathcal{X}$  and return  $z$  such that  $G(z) = x$ . This learned pseudo-inverse to the generator can be used to project any image  $x$  into the range of the generator.

### 3.3. Relaxing the Constraints

Returning to Bora et al. [17], the authors note that with increasing compressed sensing measurements, the algorithm's performance saturates rather than continuing to improve. They hypothesise that this occurs when the ground truth is not in the range of the generator. One could consider relaxing the constraint that the solution is in the range of the generator, such as in (10). More explicitly, set  $x = G(z) + u$  for some  $u \in X$ , see (11).

The addition,  $u$ , can be restricted to be small, for example by setting  $R_u(u) = \|u\|_2^2$ , see (10), or sparse under some sparsifying transform,  $B$ , e.g.  $R_u(u) = \|Bu\|_1$  [28]. Hegde [41] also restrict  $\|B^T u\|_0 \leq l$  for some constant  $l$ .

### 3.4. Additional regularisation

Additional regularisation on  $z$  is given by  $R_z$  in (9), (10) and (11). For example, we have seen,  $R_z(z) = \|z\|_2^2$  [17, 12], or  $\iota_{[-1,1]^{\dim z}}(z)$  [88]. Often, the regularisation matches the prior on the latent space used in generator training.

Menon et al. [61] discuss that  $R_z(z) = \|z\|_2^2$  forces latent vectors towards the origin. However, most of the mass of the  $n$ -dimensional Gaussian prior on their latent space is located near the surface of a sphere of radius  $\sqrt{n}$ . Instead, they use a uniform prior on  $\sqrt{\dim \mathcal{Z}} \mathcal{S}^{\dim \mathcal{Z}-1}$ . This idea has also been explored for interpolations in the latent space [94]. In addition, the prior on the latent space may not be a good model for the post-training subset of  $z$  that maps to feasible images. For a VAE there may be areas of the latent space that the generator has not seen in training. For a GAN, there could be mode collapse. In each model, we could have directions or dimensions in the latent space that provide no meaningful difference in the image space. A few recent papers consider how to find the post training latent space distribution [25, 13].

Other regularisation choices could be based on features of the image,  $x = G(z)$ . For example VanVeen et al. [89] use  $R_z(z) = TV(G(z))$ . Total variation is well established for image reconstruction [79, 2].

For a GAN generator, it is possible to take the regularisation term to be the same as the generator loss  $R_z(z) = \log(1 - D(G(z)))$ . This regulariser utilises the discriminator,  $D$ , which has been trained to differentiate generated from real data. Examples include inpainting [97, 52] and reconstruction from an unknown forward model [8].

The softly constrained approach to restricting  $x \in \mathcal{X}$  to  $Range(G)$  in (10) is similar to the approaches of [38, 69, 67, 22, 32, 75]. For  $G(\omega, \cdot) \circ E(\theta, \cdot) : \mathcal{X} \rightarrow \mathcal{X}$  an encoder–decoder network take  $R_G(x) = \|x - G(E(x))\|_2^2$ . The idea is that this regulariser approximates the distance between  $x$  and the ideal data manifold. It is also coercive, giving some useful mathematical properties [67].

Another use of the encoder for regularisation takes  $R_x(x) = \|E(x)\|$  for some norm [66, 67], usually the 2-norm to match the standard normal prior on the latent space. This regulariser could be seen as a proxy for a probability density on the image space, considering images to be more probable when the corresponding latent vector is close to the origin. However, note that the encoder is not an inverse to the generator, which is likely not invertible.

In all cases where an encoder or discriminator is used outside of training, note that they may be useful for  $x$  on or close to the ideal data manifold, however for areas rarely seen in training, there is little understanding as to how they might behave.



### 3.5. Choice of Generative Model

Variations on VAEs and GANs are the most common generative model choice but there are also some efforts to use or design generative models to have better properties. We will consider desired properties of generative models in more detail in Section 4.

An InfoGAN [23] is a GAN additionally trained to maximise the mutual information between sections of the latent space and the generated signals, giving more structure in parts of the latent space. Applied to inverse problems, some experiments [95] give favourable results for an InfoGAN over a more standard direct convolutional GAN [76]. Obmann et al. [70] encourage a sparse latent space representation and pair this with a sparse regulariser, for example,  $R_z(z) = \|z\|_q^q$  where  $q < 2$ . Models such as sparse autoencoders [59] may also be useful for encouraging sparsity.

Generative models outside of the AE, VAE and GAN families have also been considered for regularisers in inverse problems. Autoregressive models [26] generate individual pixels based on a probability distribution conditioned on previously generated pixels. Training and optimisation is practically slow.

Normalising flows and, more generally, invertible neural networks [45] are designed to be bijective, with forward or inverse mappings efficiently computable with a tractable Jacobian. A recent invertible neural network example is a GLOW network (Generative flow with invertible  $1 \times 1$  convolutions) [49] which has been used in regularisation of the form  $R_G(x) = \|G^{-1}(x)\|_2^2$  [66].

### 3.6. Other Approaches

There are a number of ideas that are linked to earlier discussions in this Section but we will not cover in detail.

Both conditional generative models [4, 73, 96, 58] and CycleGAN [99] take observed data as an input, generating a reconstruction. CycleGANs, in particular, can be useful in inverse problems where the forward model is unknown [71, 84]. The lack of lower dimensional latent space and training based on a a particular forward model makes them out of scope for this article.

We do not consider work that uses untrained generative models e.g. Deep Image Priors [89, 54, 29] or Holler and Habring [37]. As described in Lempitsky et al. [54] the idea is that the structure of a generator network, prior to any learning, captures low level image statistics. We also do not consider papers that partially retrain the generator, for example [63], or train with a specific forward model in mind [55, 47]. A major benefit of (2) is the flexibility to changes in the forward model.

Invertible neural networks and normalising flows are a growing field of generative modelling [49]. They require that the dimension of the latent space must be equal to the dimension of the image space, violating our assumption that the ground truth data lies on a lower dimensional manifold. They have the ability to provide a generated distribution with tractable density,  $p_G$ , that can be evaluated for any  $x \in \mathcal{X}$ . Utilising this additional information is a possible future research direction.

## 4. Generative Model Evaluation

Typically the aim of a generative network has been to produce high fidelity images and indeed there has been some good success with this, see for example [48, 43]. However, the success of (2) relies not just on the ability of the generator to produce a few good images but to be able to produce every possible feasible image. In this Section, we discuss desired properties for a generator trained for use in inverse problems, explore possible methods to test these properties and demonstrate these methods on three different generative models trained on two different datasets.

### 4.1. Desired Properties

To evaluate a generative model, in the context of inverse problems, we consider two overall aims which we will go on to further decompose:

- A** That samples from the generator are similar to those from the target distribution.
- B** That, given a forward model and an observation, the image in the range of the generator that best fits the observation can be recovered using descent methods.

We split aim A into a set of objectives:

- A1** The generator should be able to produce every possible image in the target distribution. That is, for all  $x \in \mathcal{X}$  such that  $x$  is similar to images in the training dataset, there exists  $z \in \mathcal{Z}$  such that  $G(z) = x$ .
- A2** The generator should not be able to produce images far from the target distribution. That is, for all  $x \in \mathcal{X}$  such that  $x$  is not similar to images in the training dataset, then there does not exist  $z \in \mathcal{Z}$  such that  $G(z) = x$ .

A1 includes that the generator should be robust to mode collapse and that the model should not trivially over-fit to the training data but also be able to generate similar images in the training distribution.

In the probabilistic case, with a prior over the latent space, objective A becomes:

- A** That samples from the latent space, when mapped through the generator, will produce samples that approximate a target distribution. We should have that  $d(P^*, P_G)$  is small for some distance measure  $d$ .

We also note that in the probabilistic case, A1 and A2 are not independent. Probability mass integrates to one, so, by assigning probability mass to parts of the image space close to the target distribution, it is less likely that images far from the target distribution can be generated. In the probabilistic case, a third Property is added:

- A3** The generator should map high probability vectors in the latent space distribution to high probability images in the target distribution.

It is possible that A1 and A2 are satisfied but not A3. Note that these properties may not be possible to achieve for a given dataset.

We define two properties required but potentially not sufficient for Property B, these are

**B1** The generator should be smooth with respect to the latent space,  $\mathcal{Z}$ .

**B2** The area of the latent space,  $\mathcal{Z}$ , that corresponds to feasible images should be known.

B1 ensures that gradient-based optimisation methods can be used. Continuity is also desirable: we wish that, in some way, points close in the latent space should produce similar images. B2 considers that we need to have a distribution on or subset of  $\mathcal{Z}$  to sample from in order to use the generator to sample images. This distribution may not be equal to any priors on the latent space used during training.

#### 4.2. Generative Model Evaluation Methods

There are a wide range of existing generative model evaluation methods [18], focused mostly on Property A.

For Property A2, that no unfeasible images should be generated, the *average log likelihood* [33] of the test data under the generated distribution,  $\frac{1}{|\mathcal{X}_{\text{test}}|} \sum_{x \in \mathcal{X}_{\text{test}}} \log p_G(x)$ , is a natural objective to maximise. There is evidence, however, that the likelihood is generally unrelated to image quality [86]. Estimating the likelihood in higher dimensions is often not computationally feasible and approximations come with their own issues [86].

In an effort to check Property A1 that the generator can produce all feasible images, Arora et al. [10] use a ‘*Birthday paradox*’ technique to estimate the size of the support of the generated distribution to compare with the expected size. A low support size would suggest mode collapse. They find the minimum sample size  $S$  of generated data such that they are more likely than not to find duplicates and estimate the support size to be  $S^2$ . Practically, finding duplicates is not straightforward and may need to be done manually.

The probabilistic version of A requires that  $d(P^*, P_G)$  is small for some distance measure  $d$ . When choosing a distance measure, note that we do not have access to either distribution, just samples from them. The *Frechet Inception Distance (FID)* [42] and *Maximum Mean Discrepancy (MMD)* [35] encode samples of real and generated data in a lower dimensional space using any neural network, usually one trained for classification. In this lower dimensional space FID takes the Wasserstein distance between multivariate Gaussians fitted to the samples. MMD takes the difference between the mean of a kernel function applied to the two sets of samples [34]. In both cases a model that simply stores all training samples would score perfectly. The embedding used for the test is likely to have the same problems and drawbacks as the embedding learnt by the generative model the test is meant to evaluate.

A number of tests train a neural network to distinguish between real test data and generated data. Failure to classify the two is a success of the generative model.

The *Wasserstein Critic* [9] provides an approximation of the Wasserstein distance between  $P^*$  and  $P_G$ . *Classifier two-sample tests* [56] use the classification scores to run a statistical test, with null hypothesis that  $P^* \equiv P_G$ . For testing a GAN, the new discriminator is unlikely to be able to pick up failures that the original discriminator, used in training, missed.

Another possible option is to calculate the earth movers distance (EMD) [78], a discretised version of the Wasserstein-1 distance, between samples from the two distributions. Although, simple and computationally tractable, a model that stores all training data would perform well.

Property B is less explored in the literature. The most natural approach would be to take an image not seen by the generator, and using descent methods find the latent vector,  $z$ , which best reconstructs the image and compare the original and reconstruction. A close reconstruction would also provide evidence for Property A1. With these found latent vectors, visualising their locations could check Property B2.

To test the smoothness of the generator with respect to the latent space, Property B1, many previous generative model papers, including the original GAN and VAE papers [33, 50], attempt to interpolate through the latent space, visualising the output and hoping for smooth transitions through feasible images. Of course, with a large latent space, looking at interpolations along a small distance in just a few directions will not be sufficient to confirm smoothness, but the hope is that some intuition would be gained. Interpolations leading to unfeasible images would also be a failure of Property A2.

### 4.3. Numerical Experiments

In this Section, we evaluate AE, VAE and GAN models against the desired properties given in Section 4.1. We consider experiments on two datasets. Firstly, a custom made `shapes` dataset with 60,000 training and 10,000 test  $56 \times 56$  grey-scale images. Each image consists of a black background with a grey circle and rectangle of constant colour. The radius of the circle; height and width of the rectangle; and locations of the two shapes are sampled uniformly with ranges chosen such that the shapes do not overlap. This dataset is similar to datasets used in [73]. For examples, see the ground truth images in Figure 3.

Secondly, the MNIST dataset [53] consists of  $28 \times 28$  grey-scale images of handwritten digits with a training set of 60,000 samples, and a test set of 10,000 samples. For examples, see the ground truth images in Figure 2.

We consider the three methods of training a generator discussed in Section 2: autoencoders (AEs), variational autoencoders (VAEs) and Wasserstein generative adversarial networks (WGANs). Architectures were chosen based on the implementations in Kingma et al. [50] and Gulrajani et al. [36] for the VAE and WGAN, respectively, with efforts to use the same generator network in all three models for comparison. Useful architecture guidelines for generators based on convolutions are given by Salimans et al. [81]. More architecture details are given in the Appendix.

All models have gone through a similar amount of limited optimisation of hyperparameters, including: the noise level  $\rho$  in the VAE decoder (8); the latent dimension; number of layers; choice of convolution kernel size; drop out probability; leaky ReLU coefficient and learning rate. In order to select hyperparameters we manually inspected generated images and training image reconstructions. This process of choosing hyperparameters could be sped up in future by considering automatic machine learning procedures.

Models were built and trained using Tensorflow [1] in Python and made use of the Balena High Performance Computing (HPC) Service at the University of Bath. The models were trained using a single Dell PowerEdge C8220X node, with two Intel E5-2650 v2 CPU, 64 GB DDR3-1866 MHz Memory and an Nvidia K20X GPU (6 GB memory). The **MNIST** and **shapes** VAE models taking approximately 25 and 45 minutes to train, respectively.

#### 4.4. Reconstructing a Test Dataset

Property A1 asks that the generator is able to produce every image in the target distribution, and this is tested using an unseen test dataset. Gradient descent with backtracking line search (Algorithm 1) is used to approximately solve

$$z^*(x) \in \arg \min_z \|G(z) - x\|_2^2, \quad (15)$$

for each  $x \in \mathcal{X}_{\text{test}}$ . For the AE and VAE, the Algorithm is initialised at the (mean) encoding of the test image. For the GAN, there is no encoder to give an initial value of  $z$  and instead a random point in the latent space is chosen from a standard normal distribution. We find empirically, especially for the GAN, that different initialisations lead to different solutions. We take 4 different initialisations for the the GAN optimisation, but this could be easily parallelised to take more initialisations.

It is important that the generators are able to reproduce images across the full range of the image distribution. Figure 1 shows the values of  $d(G(z^*(x)), x)$  for different choices of distance  $d$  and plotted as a histogram for all  $x \in \mathcal{X}_{\text{test}}$ . We consider 4 different metrics: normalised root mean squared error (NRMSE,  $d_{\text{NRMSE}} = \frac{\|x^* - x\|_2}{\|x\|_2}$ ), peak signal-to-noise-ratio (PSNR, see definition 3.5 in [19]), structural similarity index (SSIM, [93]) and 1-norm. Figures 2 and 3 also show reconstruction examples for **MNIST** and **shapes** datasets, respectively, for the three different models.

We see that, for both the **MNIST** and **shapes** dataset, the AE and VAE have almost identical reconstruction results. Figures 2 and 3 show that visually the AE and the VAE provide reasonably good reconstructions across the range of the test set. The GAN results are worse in each metric for **MNIST** data. For the **shapes** dataset the difference in results between the three generative models is less stark and the GAN has slightly better PSNR values. Visually, in Figures 2 and 3, the GAN has a much wider range of reconstruction errors, with on average higher errors but some good, and particularly poor reconstructions. A poor reconstruction does not necessarily imply that the image is not in the range of the generator, but perhaps instead that we have not

found the correct encoding. The lack of encoder in the GAN, makes this potentially more challenging. Despite this caveat, the non-circular objects in the GAN results for the `shapes` dataset could be a failure of the discriminator to detect circles.

In Figure 1, NRMSE values are given for three different latent dimensions to show that the results are not sensitive to small changes in latent dimension. Latent dimensions of 8 and 10 for MNIST and `shapes` datasets are chosen as a good middle ground for comparison purposes in the rest of this paper.

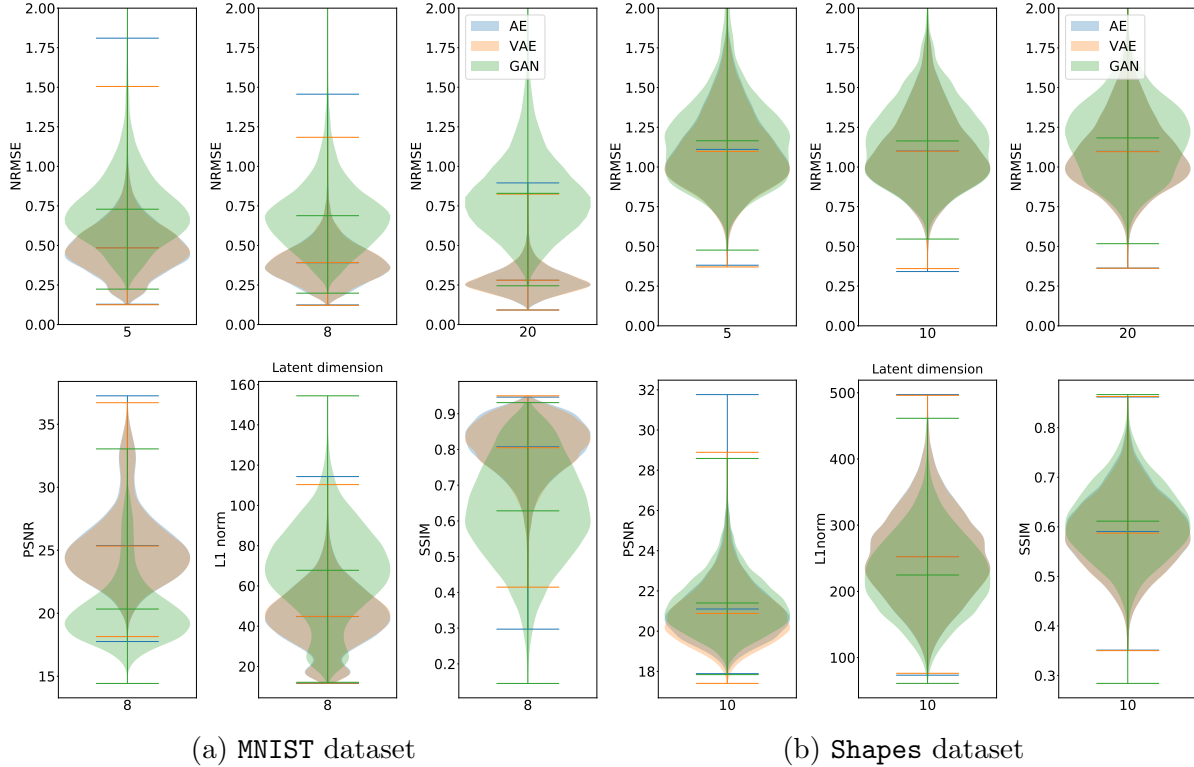


Figure 1: The values of  $d(G(\arg \min_z \|G(z) - x\|_2), x)$  for different choices of distance  $d$  and plotted as a histogram for all  $x \in \mathcal{X}_{\text{test}}$ . Note the brown colour is the result of the overlapping orange (VAE) and blue (AE).

#### 4.5. Distance Between $P_G$ and $P^*$

To investigate Property A3, the earth movers distance (EMD) [78] is calculated between the generated and the data distribution. The EMD is a discretised version of the Wasserstein-1 distance. For image set  $\mathcal{X}_{\text{test}} = \{x_1, \dots, x_N\}$  and generated images  $G(z_i)$  where  $z_i \sim \mathcal{N}(0, I)$  for  $i = 1, \dots, N$ , calculate

$$\min_f \sum_{i,j=1}^N f_{i,j} \|x_i - G(z_j)\|_2^2, \quad s.t. \quad 0 \leq f_{i,j} \leq 1, \quad \sum_{i=1}^N f_{i,j} = 1, \quad \sum_{j=1}^N f_{i,j} = 1. \quad (16)$$

The EMD is calculated using the Python Optimal Transport Library [30] with  $N = 10,000$ , the full test set. For the purpose of comparison between datasets the

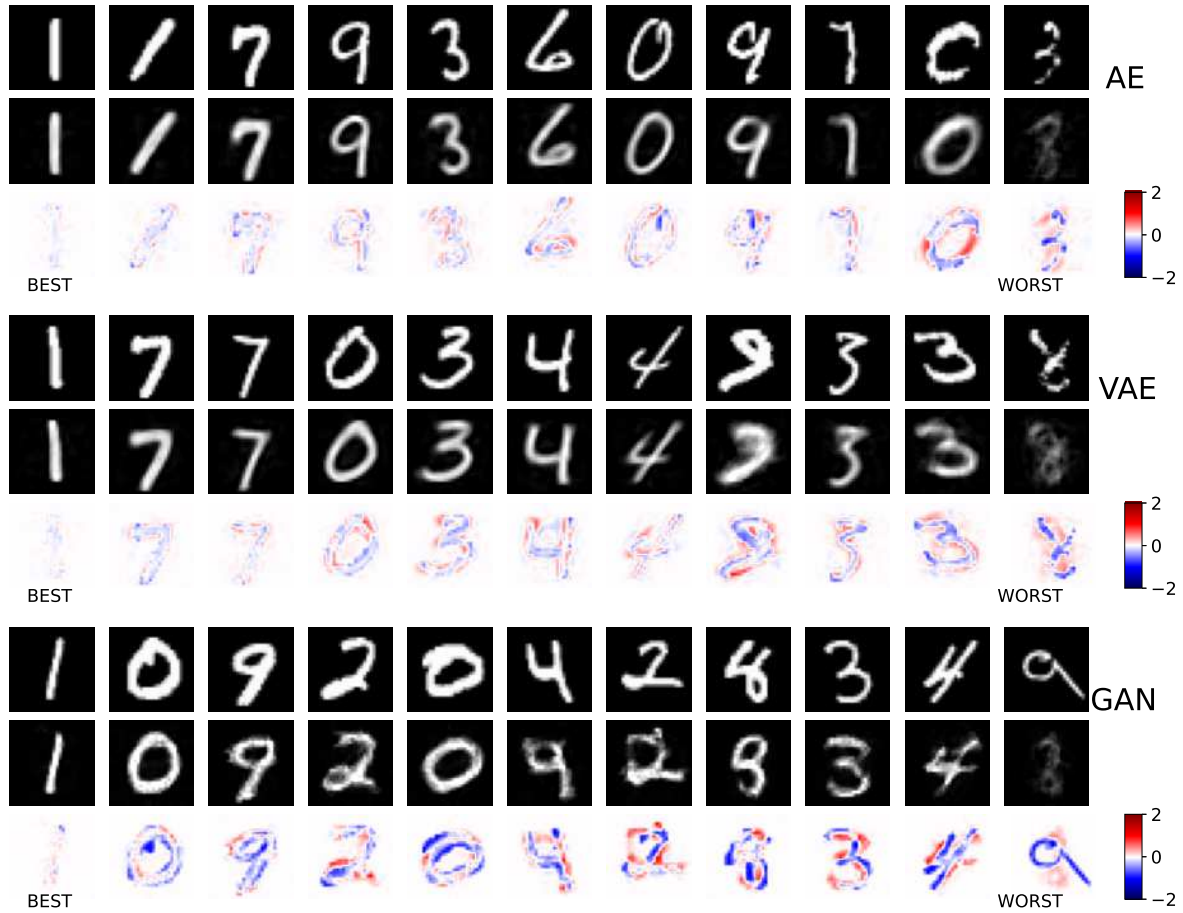


Figure 2: Example reconstructions for the MNIST dataset with a ten-dimensional, AE, VAE and GAN. In each sub-figure, the top row shows the original, second row the reconstruction and third row the error. The 11 images were chosen as the deciles of the NRMSE.

EMD is normalised by the average of  $\|x\|_2^2$  over the test set.

The results are given in figures 4(a) and 4(c). In both the MNIST and **shapes** examples, the VAE does substantially better and behaves consistently across the latent dimensions. The AE is added to this plot for comparison purposes but, as there is no prior on the latent space for an AE,  $z_i \sim \mathcal{N}(0, I)$  may not be the best choice to sample from.

#### 4.6. Visualisations of the Latent Space

Property B2 requires that the area of the latent space that maps to feasible images is known. There is no prior on the latent space enforced for AEs and a  $\mathcal{N}(0, I)$  prior is imposed for VAEs and GANs.

In figures 4(b) and 4(d), gradient descent with backtracking (Algorithm 1) is used to approximate (15), finding a latent vector  $z^*(x)$  for each  $x \in \mathcal{X}_{\text{test}}$ . For comparison,

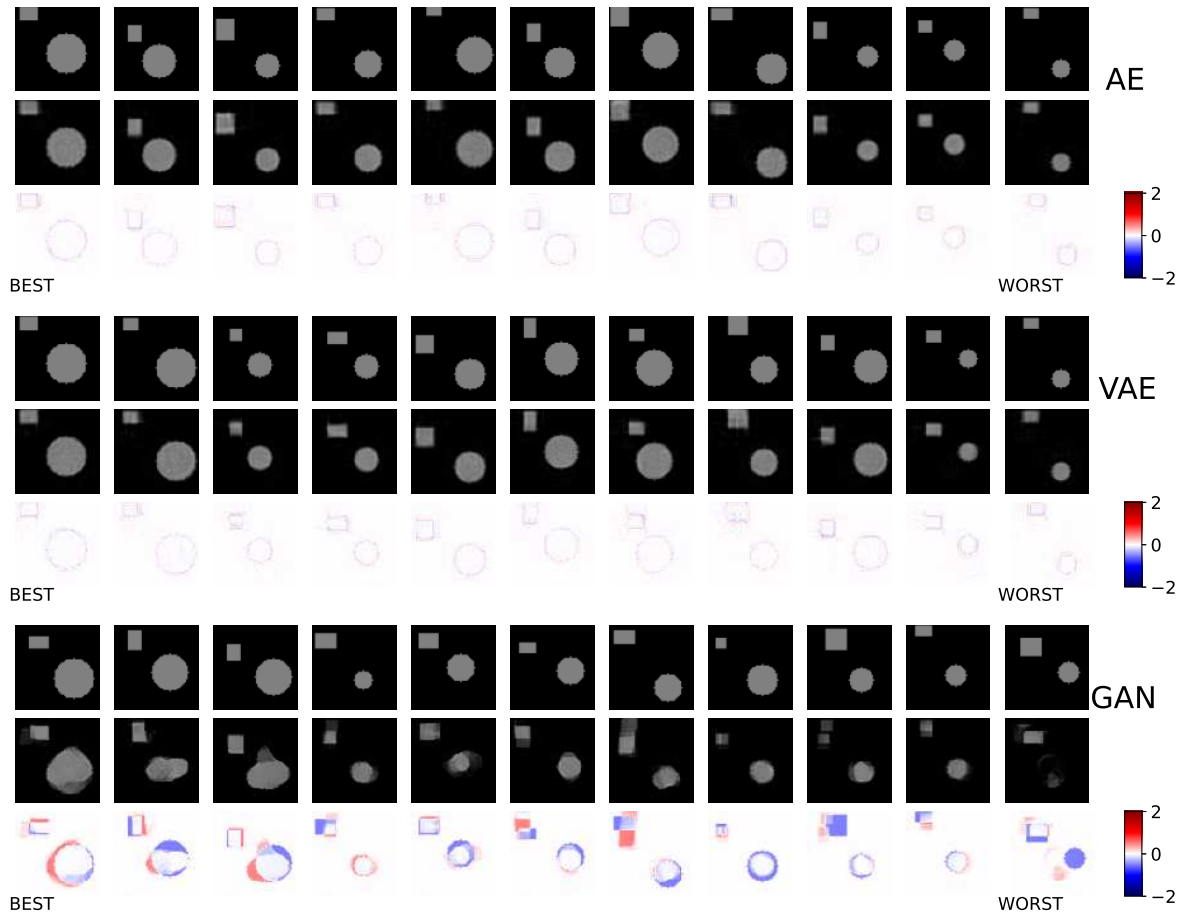


Figure 3: Example reconstructions for the `shapes` dataset with a ten-dimensional, AE, VAE and GAN. In each sub-figure, the top row shows the original, second row the reconstruction and third row the error. The 11 images were chosen as the deciles of the NRMSE.

the values  $z^*(x)$  for the test set and 10,000 random Gaussian  $\mathcal{N}(0, I)$  vectors are then randomly projected into 2 dimensions.

The encodings in the latent space match the prior  $\mathcal{N}(0, I)$  well for VAEs. For the GAN examples, the encodings match the prior, but, noting the poorer reconstruction results discussed in Section 4.4, the encoded distributions might match but the generated images may be poor.

For AEs, there are examples, especially for low latent dimensions, where the area covered by the encodings does not match a  $\mathcal{N}(0, I)$  distribution. If using the decoder of the AE as a generator, without investigation, then there is no natural choice for values of  $z$  to sample from.



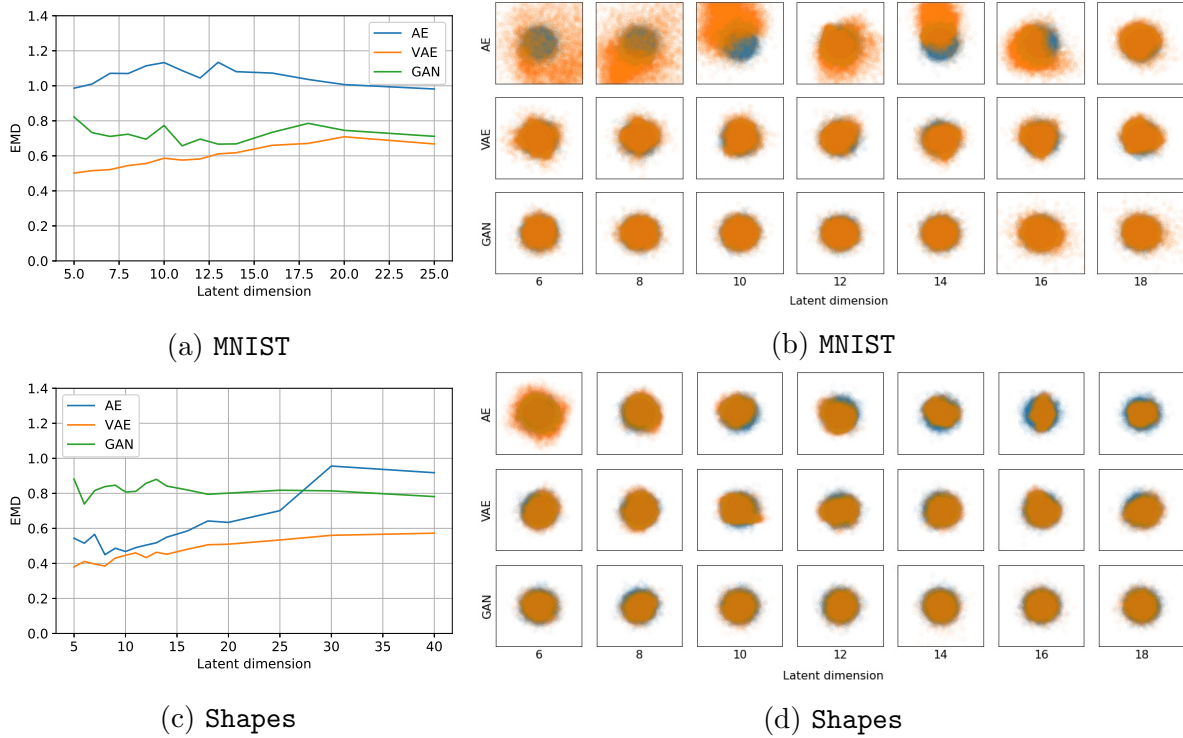


Figure 4: On the left, EMD between the test dataset and samples from a trained generator. On the right projections into 2D of the latent space encodings of a test dataset, in orange, and standard normal vectors, blue.

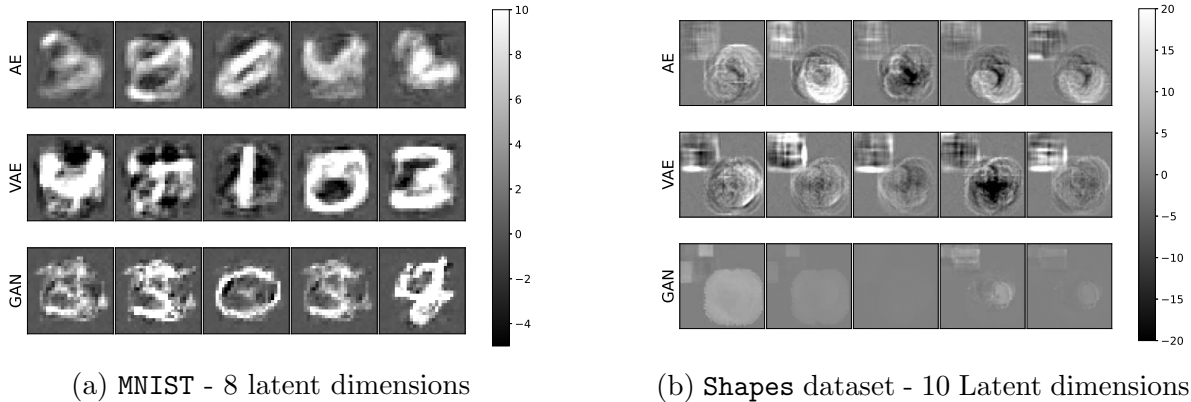


Figure 5: Images generated far from the high-probability region of the prior distribution, demonstrating the importance of Property B2.

#### 4.7. Generating Far from the Latent Distribution

A known latent space gives known areas to sample from. Figure 5 shows image examples generated far from these locations. In each case the generated images look poor compared to the training distributions and perhaps are some sort of average image. This plot emphasises the importance of Property B2, and highlights the problem of using an AE, where there is no prior available, for generating new images.

#### 4.8. Interpolations in the Latent Space

Property B1 asks that the generator is smooth with respect to the latent space. The continuity of the mapping is determined by the choice of the architecture but, for descent methods to be successful, it would be beneficial for there to be no large gradients or jumps between points in the latent space. Points close in the latent space should be mapped to similar images. Property A2 also asks that no unfeasible images should be produced when moving through the latent space. To investigate these two properties, Figure 6 shows interpolations between points in the latent space. We take three images from the test data,  $x_1, x_2$  and  $x_3$ , find  $z_1, z_2$  and  $z_3$ , their encodings in the latent space, using (15) and then plot interpolations  $G(z_1 + \alpha_2(z_2 - z_1) + \alpha_3(z_3 - z_1))$  for  $\alpha_1, \alpha_2 \in [0, 1]$ .

The AE and VAE, Figures 6(a), 6(b), 6(d) and 6(e), do reasonably well. For a VAE, the prior on the latent space and the KL divergence acting as a regulariser attempts to enforce some smoothness in the latent space so it is surprising to see similar results for the AE, despite the lack of prior or regularisation on the latent space. In some cases for example in Figure 6(b) for the VAE and Figure 6(a) for the AE, the images look more like pixel wise interpolation with unfeasible images in the intermediary values. We note that for the VAE, although there is a prior, generation of feasible images may not be possible from every point in the prior.

For the GAN, the prior on the latent space should ensure that points sampled from  $\mathcal{N}(0, I)$  should map to feasible images but there is no requirement that similar locations map to similar images. For both dataset examples the GAN seems to do worst, with the large jumps as predicted, but also some unfeasible images. In Figure 6(f) there are a whole range of images that contain no rectangle, examples of which were never in the training set. These images could be evidence of a discriminator failure: the discriminator has not yet learnt that these images are ‘fake’.

#### 4.9. Discussion

As expected, none of the three models, AE, VAE and GAN, fulfil objectives A and B fully. For A, the GAN does poorly in the reconstruction results of Figures 2, 3 and 1. There is evidence of mode collapse, where parts of the training data are not well reconstructed and discriminator failure, where the images produced are not realistic, see Figures 3 and 6. The VAE does consistently better, demonstrated by the lower earth movers distance between generated and test data in Figure 4. The lack of prior on the AE, and thus a known area of the latent space to sample from, is a problem. Figure 5 demonstrates that sampling from the wrong area of the latent space gives poor results.

Pulling apart the cause of a failure to recover an image is difficult. It could be that the image is not in the range of the generator, a failure of objective A, or that the image is in the range of the generator but the image cannot be recovered using descent methods, a failure of objective B. The mathematical properties of continuity or differentiability of a network, depend on the architecture. The interpolations in Figure

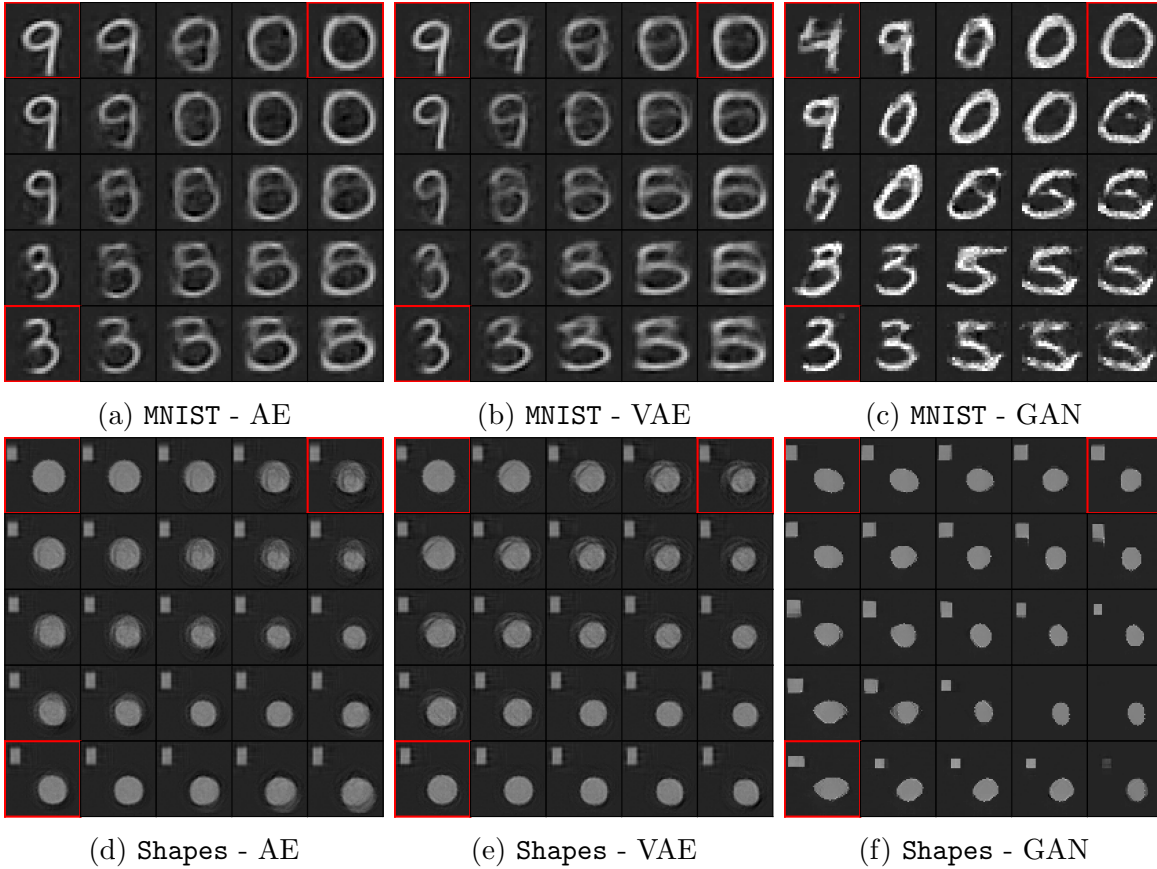


Figure 6: Interpolation ability of an AE, VAE and GAN. The highlighted top left, bottom left and top right latent space values were chosen close to the test dataset and the other images are computed via linear combinations in the latent space. Smooth interpolations between images would support B1 and feasible images generated from all points in the latent space would support A2.

6 show some evidence of large jumps between images in the GAN cases, but in general the interpolations are reasonable, Property B1. For both the GAN and the VAE, in Figure 4, the encodings of the test images in the latent space seem to match the prior, objective B2.

## 5. Numerical Applications to Inverse Problems

In this Section, we test the AE, VAE and GAN models, evaluated in the previous Section, on inverse problems.

The datasets are the same as before, however, in addition, we train a VAE to produce Knee MRI Images. The VAE architecture is based on Figure 1 in Narnhofer et al. [63], and is detailed in the Appendix. The NYU fastMRI knee dataset contains data 796 fully sampled knee MRI magnitude images [51, 98], without fat suppression. We extract 3,872 training and 800 test ground truth images from the dataset, selecting

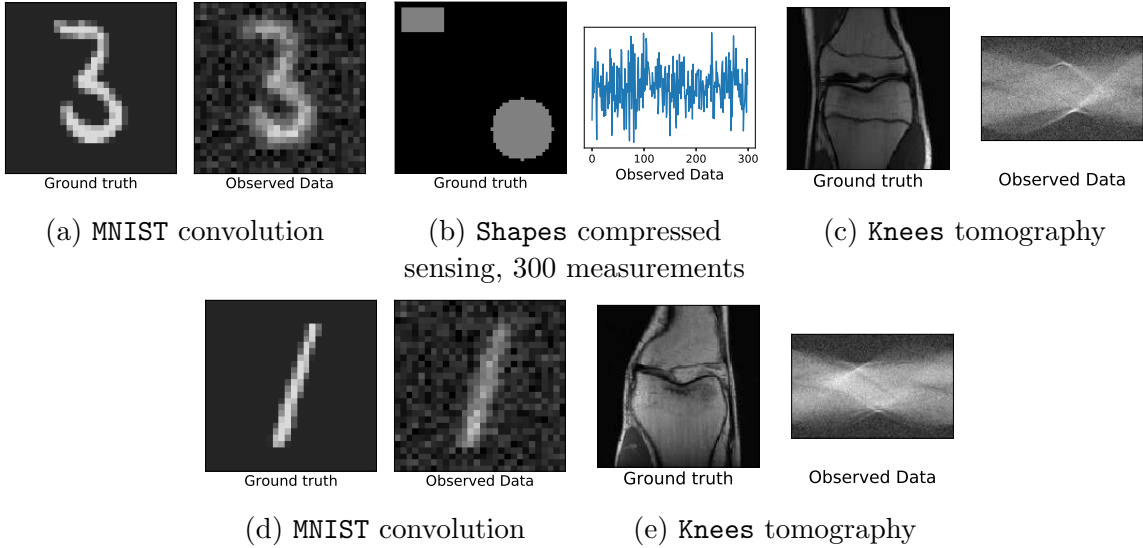


Figure 7: Data and ground truth images for Figures 8, 9, 11, 14 and 15. The labels **MNIST**, **Shapes** and **Knees** refer to the dataset. The observed data has added white noise with standard deviation 0.1, 0.05, 0.02, 0.1, and 0.02 respectively.

images from near the centre of the knee, resize the images to  $128 \times 128$  pixels and rescale to the pixel range  $[0, 1]$ . The models were trained using a single Dell PowerEdge C8220X node, with two Intel E5-2650 v2 CPU, 64 GB DDR3-1866 MHz Memory and an Nvidia K20X GPU (6 GB memory). The **knee** VAE models taking approximately 12 hours to train.

Three inverse problems are considered. Firstly *tomography*, the X-ray transform [64] with a parallel beam geometry. Secondly, *deconvolution* with a  $5 \times 5$  Gaussian kernel. Lastly, *compressed sensing* measurements give an under-determined linear system where  $y = Ax$  and  $A$  is a  $\mathbb{R}^{m \times d}$  Gaussian random matrix,  $x \in \mathbb{R}^d$  is a vectorised image and  $d \gg m$ , see for example [27]. The ground truth and data examples are given in Figure 7. In each case zero-mean Gaussian noise with standard deviation  $\sigma$  is added to the data. The inverse problem aspects were implemented using the operator discretisation library (ODL) [5] in Python, accessing scikit-learn [74] for the tomography back-end.

To match the literature themes, consider three different variational regularisation methods written in the form of (2) as

$$\min_x \frac{\|Ax - y\|_2^2}{2\sigma^2} + \lambda R_G(x) \quad (17)$$

with different choices of generative regulariser

$$R_G(x) = \min_{z \in \mathcal{Z}} \iota_{\{0\}}(G(z) - x) + \|z\|_2^2, \quad (18)$$

$$R_G(x) = \min_{z \in \mathcal{Z}} \|G(z) - x\|_2^2 + \mu \|z\|_2^2, \quad (19)$$

$$R_G(x) = \min_{z \in \mathcal{Z}, u \in \mathcal{U}} \iota_{\{0\}}(G(z) + u - x) + \|u\|_1 + \mu \|z\|_2^2. \quad (20)$$

The methods are called *hard constraint*, *relaxed constraint* and *sparse deviation* respectively. For comparison we consider regularisers independent of the generator: *Tikhonov* regularisation,  $R_G(x) = \|x\|_2^2$ , for the convolution and tomography examples (Figures 7(a), 7(c)–7(e)) and Total Variation (*TV*) regularisation [79], for the compressed sensing example (Figure 7(b)).

Each variational problem requires a slightly different algorithm. *Hard constraint* (18) and *Tikhonov* are optimised using Gradient Descent with backtracking line search, Algorithm 1. *TV* regularisation is implemented using the Primal Dual Hybrid Gradient method [21]. To solve *relaxed constraint* (19), alternating gradient descent with backtracking is used, see Algorithm 2. Finally, for *sparse deviations* (20), the 1-norm is not smooth, and so Proximal Alternating Linearised Minimisation (PALM) [16] with backtracking is used, see Algorithm 3. Initialisations are chosen from a standard normal distribution.

---

**Algorithm 1** Gradient Descent with Backtracking to solve  $\min_z f(z)$ .

---

- 1: Initialise  $z_0$ ,  $L > 0$ ,  $0 < \eta_0 < 1$ ,  $\eta_1 > 1$ .
  - 2: **for**  $i = 1, \dots, K$  **do**
  - 3:   Let  $\tilde{z}(L) := z_{i-1} - \frac{1}{L} \nabla f(z_{i-1})$
  - 4:   **while**  $f(\tilde{z}(L)) \geq f(z_{i-1}) - \frac{1}{2L} \|\nabla f(z_{i-1})\|_2^2$  **do**
  - 5:      $L = L\eta_1$
  - 6:    $z_i = \tilde{z}$  and  $L = L\eta_0$ .
- 

---

**Algorithm 2** Alternating Gradient Descent with Backtracking to solve  $\min_{z,x} f(z, x)$ .

---

- 1: Initialise  $z_0$  and  $x_0$ ,  $L_z > 0, L_x > 0$ ,  $0 < \eta_0 < 1$  and  $\eta_1 > 1$
  - 2: **for**  $i = 1, \dots, K$  **do**
  - 3:   Let  $\tilde{z}(L_z) := z_i - \frac{1}{L_z} \nabla f(z_i, x_i)$
  - 4:   **while**  $f(\tilde{z}(L_z), x_i) \geq f(z_i, x_i) - \frac{1}{2L_z} \|\nabla f(z_i, x_i)\|_2^2$  **do**
  - 5:      $L_z = L_z\eta_1$
  - 6:   Let  $z_{i+1} = \tilde{z}(L_z)$  and then  $L_z = L_z\eta_0$
  - 7:   Let  $\tilde{x}(L_x) := x_i - \frac{1}{L_x} \nabla f(z_{i+1}, x_i)$
  - 8:   **while**  $f(z_{i+1}, \tilde{x}(L_x)) \geq f(z_{i+1}, x_i) - \frac{1}{2L_x} \|\nabla f(z_{i+1}, x_i)\|_2^2$  **do**
  - 9:      $L_x = L_x\eta_1$
  - 10:   Let  $x_{i+1} = \tilde{x}(L_x)$  and  $L_x = L_x\eta_0$
- 

The choice of regularisation parameter will vary depending on the inverse problem and data. To find a suitable choice, parameters are often chosen according to the Morozov discrepancy principle [87], taking the largest values of the parameters such that  $\|y - Ax\|_2^2$  is less than the expected value of the noise,  $\dim \mathcal{Y} \cdot \sigma^2$ . In this work, a range of parameter values are plotted alongside the Morozov discrepancy level for comparison.

---

**Algorithm 3** PALM with backtracking to solve  $\min_{z,u} f(z, u) + g_1(z) + g_2(u)$ . Define  $\text{prox}_h(z) = \arg \min_x \{h(x) + \frac{1}{2}\|x - z\|_2^2\}$ .

---

- 1: Initialise  $z_0, u_0, L_z > 0, L_x > 0, 0 < \eta_0 < 1$  and  $\eta_1 > 1$ .
  - 2: **for**  $i = 1, \dots, K$  **do**
  - 3:     Let  $\tilde{z}(L_z) := \text{prox}_{\frac{1}{L_z}g_1}(z_i - \frac{1}{L_z}\nabla_z f(z_i, u_i))$
  - 4:     **while**  $f(\tilde{z}(L_z), u_i) > f(z_i, u_i) + \nabla_z f(z_i, u_i)^T(\tilde{z}(L_z) - u_i) + \frac{L_z}{2}\|\tilde{z}(L_z) - z_i\|_2^2$  **do**
  - 5:          $L_z = L_z\eta_1$
  - 6:     Let  $z_{i+1} = \tilde{z}(L_z)$  and then  $L_z = L_z\eta_0$
  - 7:     Let  $\tilde{u}(L_u) := \text{prox}_{\frac{1}{L_u}g_2}(u_i - \frac{1}{L_u}\nabla_u f(z_{i+1}, u_i))$
  - 8:     **while**  $f(z_{i+1}, \tilde{u}(L_u)) > f(z_{i+1}, u_i) + \nabla_u f(z_{i+1}, u_i)^T(\tilde{u}(L_u) - u_i) + \frac{L_u}{2}\|\tilde{u}(L_u) - u_i\|_2^2$  **do**
  - 9:          $L_u = L_u\eta_1$
  - 10:     Let  $u_{i+1} = \tilde{u}(L_u)$  and then set  $L_u = L_u\eta_0$
- 

### 5.1. MNIST

Reconstructions for the deconvolution problem on the MNIST dataset for the different reconstruction methods are given in Figure 8 for an 8-dim GAN. *Hard constraints* (18) give reasonable visual results for the GAN (Figure 8(b)) despite not reaching the discrepancy value. For the *hard constraints* (18) the parameter  $\lambda$  is not a traditional regularisation parameter and, as reconstructions are restricted to the range of the generator, we do not expect the data discrepancy to go to zero as  $\lambda$  decreases. In the *relaxed constraint* reconstruction (Figure 8(c)), for smaller values of  $\lambda$  the solutions tend towards a least squares solution which fits the noise and is affected by the ill-posedness of the inverse problem. The results for the *sparse deviations* from the range of the generator (20) (Figure 8(d)) in general look better than for the *relaxed constraint* reconstruction, potentially because of the choice of Gaussian noise in the inverse problem. The additional variation in the choice of  $\mu$ , as shown in the colour bar, has little effect for smaller values of  $\lambda$ .

Figure 9 again shows a deconvolution problem on the MNIST dataset. We choose the *hard constraint* (20) reconstruction for the three different models: AE, VAE and GAN. The best visual results are given by the VAE and the AE also produces reasonable reconstructions. The GAN has failed to find a good value in the latent space to reconstruct the number three. The choice of initial value of  $z$  significantly affects the outcome of the reconstruction in the GAN case. It could be that the GAN optimisation is getting stuck in a local minima.

Taking the compressed sensing inverse problem, with 150 angles, and choosing regularisation parameters to optimise PSNR over 20 test images, table 1 gives the average and standard deviation for the PSNR of 100 reconstructed MNIST digits. Due to the cartoon like nature of the MNIST digits,  $TV$  regularisation is particularly suitable,

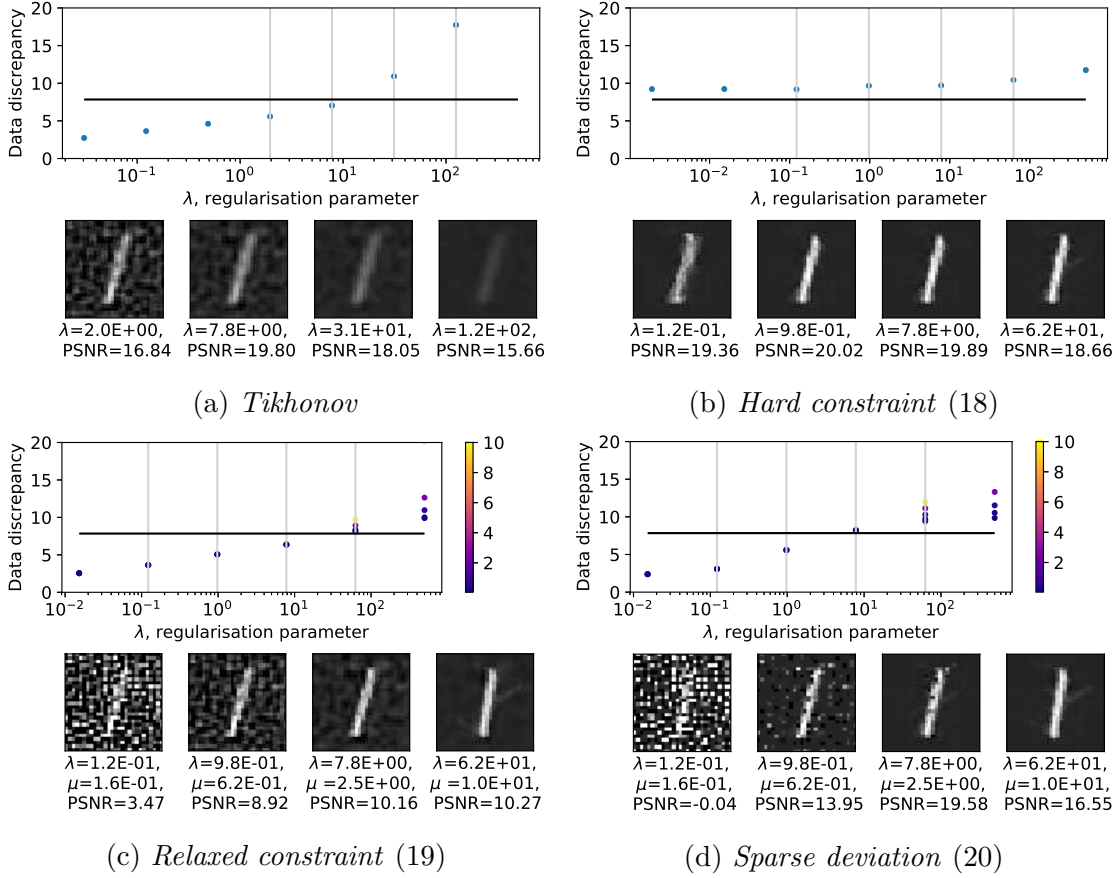


Figure 8: Solution of the inverse problem given in Figure 7(d) using an eight-dimensional GAN. The plot shows the reconstruction loss against regularisation parameter choice  $\lambda$  and a range of choices for  $\mu$ , given in the colour bar. The image plots correspond to the parameter values shown by the grey lines.

however VAE and AE *hard constraints* and VAE *soft constraints* are competitive with TV. Note the higher variance in the generative regularisers, possibly due to the generator not being able to produce all possible images or the result of the non-convex optimisation. For more context, six plots spanning the range of the reconstruction errors for the the VAE with *hard constraint* and for TV reconstruction are given in Figure 10. The generative regularisers can produce some great reconstructions, but can also fail to reconstruct a good image. This latter case could, however, be detected by considering the loss in the data space.

To give an indication of computational cost, *Tikhonov* reconstruction on the compressed sensing inverse problem on the MNIST dataset took on average 32 iterations of backtracking until the relative difference between iteration values was less than  $10^{-8}$ . In comparison, the *hard constraint* (18) and *relaxed constraint* (19) took on average 54 and 325 backtracking steps, respectively, without random restarts.

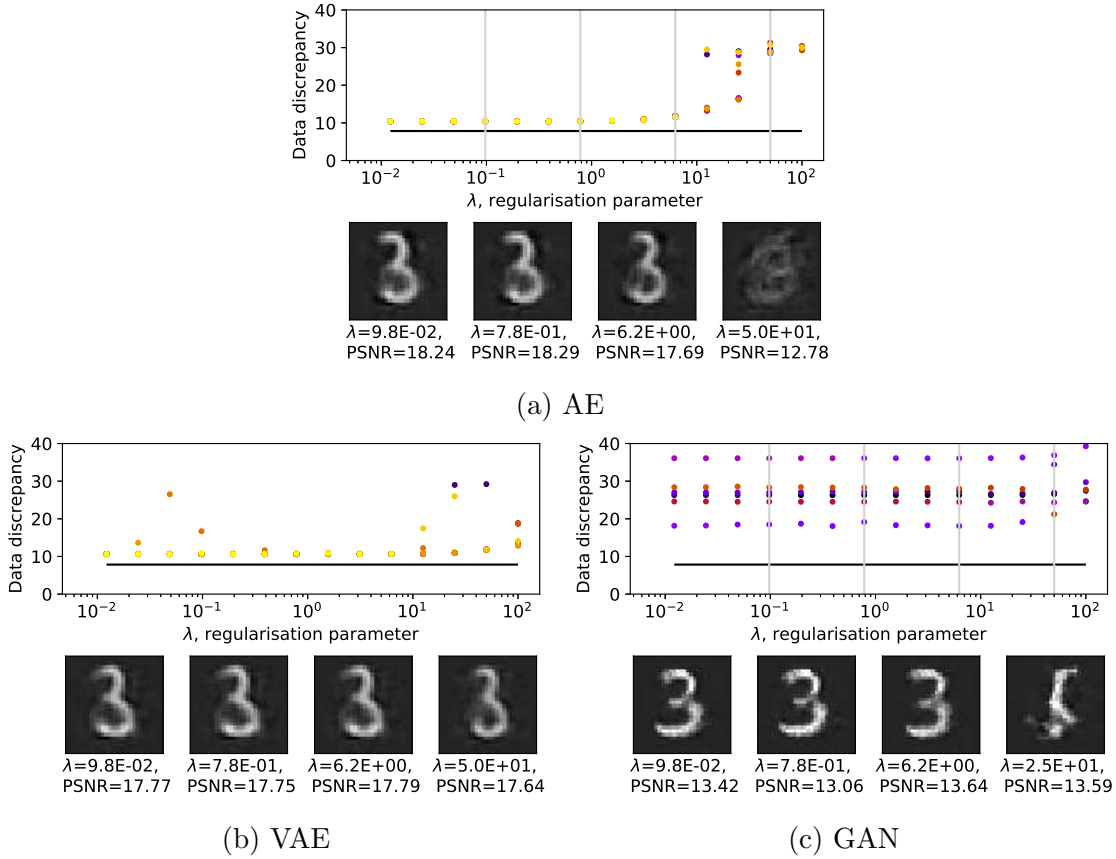


Figure 9: Comparisons between the three generators, with eight-dimensional latent space, for the inverse problem given in Figure 7(a). Reconstructions use the *hard constraint* (18) method. The plot shows the reconstruction loss against regularisation parameter choice  $\lambda$ . Ten different initialisations are chosen, depicted in different colours, which are then used for each choice of regularisation parameter. The image plots correspond to the parameter values shown by the grey lines and show the best result found for given parameters.

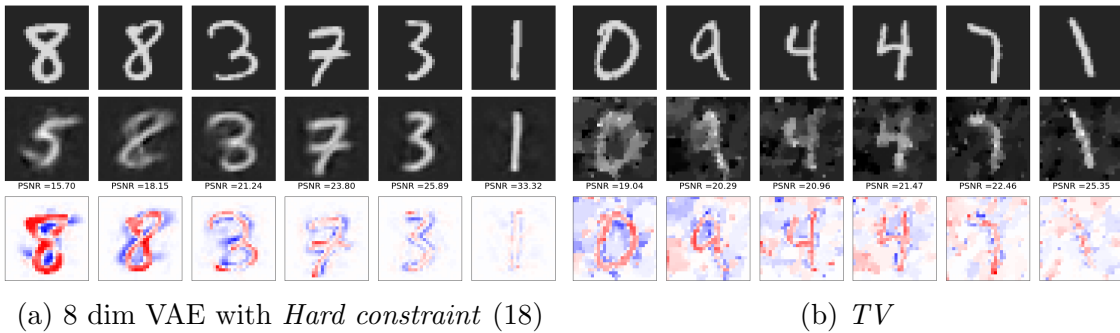


Figure 10: The worst to best reconstructions from 150 compressed sensing measurements of 100 MNIST test images. Here we compare the VAE with *Hard constraint* to *TV* reconstruction. The top line shows the ground truth, second line the reconstruction and bottom line the difference.



Method	Generative Model			
	AE	VAE	GAN	None
<i>Relaxed Constraint</i> (19)	$19.31 \pm 2.26$	$20.07 \pm 1.66$	$17.12 \pm 1.67$	
<i>Sparse Deviation</i> (20)	$19.52 \pm 2.72$	$21.08 \pm 3.16$	$17.06 \pm 2.5$	
<i>Hard Constraint</i> (18)	$21.84 \pm 4.09$	<b><math>22.33 \pm 4.17</math></b>	$16.93 \pm 2.57$	
<i>TV</i>				$21.54 \pm 1.32$

a Compressed sensing measurements (150 dimensions) of MNIST images

Method	Generative Model			
	AE	VAE	GAN	None
<i>Relaxed Constraint</i> (19)	$30.70 \pm 1.59$	$28.79 \pm 0.71$	$24.20 \pm 0.49$	
<i>Sparse Deviation</i> (20)	$33.12 \pm 0.80$	$33.09 \pm 0.89$	$22.72 \pm 1.80$	
<i>Hard Constraint</i> (18)	<b><math>33.17 \pm 0.80</math></b>	$32.92 \pm 0.95$	$22.92 \pm 2.10$	
<i>TV</i>				$29.94 \pm 0.75$

b Tomography measurements of **shapes** images

Table 1: Mean and standard deviations of PSNR values of 100 reconstructions of test images. Results compare the three different regularisers and three different methods against the unlearned *TV* reconstruction.

## 5.2. Shapes

For a second inverse problem example, Figure 11 shows an example from the **shapes** dataset with 300 compressed sensing measurements and reconstructions using a ten-dimensional AE. Reconstruction using *TV* regularisation (Figure 11(a)) gives carton like shapes in the right places, but not clear circles and rectangles. *Hard constraints* (18) (Figure 11(b)) give visually better results, although blurred compared to the ground truth and not reaching the discrepancy value. In the *relaxed constraint* case (19) (Figure 11(c)) the reconstruction fits to the noise. The results for the method allowing *sparse deviations* from the range of the generator (20) are shown in Figure 11(d) and show good reconstructions with little evidence of fitting noise. The *sparse deviation* method may work well for this example because of the relatively sparse nature of the image data. Note that the varying initialisation of the optimisation schemes does not seem to make much difference in the *hard constraint* case or for small values of  $\mu$  for the *relaxed constraint* and *sparse deviations* methods. This suggests that local minima may not be a significant problem.

Taking the tomography inverse problem (with 0.1 additive Gaussian noise), Table 1b gives the average and standard deviation for the PSNR of 100 reconstructed **shapes** images. The GAN has a particularly poor performance, suggesting that it is difficult to find the correct local minima. The AE and VAE results are all competitive with TV. Six plots spanning the range of the reconstruction errors for the the AE with *hard constraints* and for TV reconstruction are given in Figure 12. The generative regulariser gives a

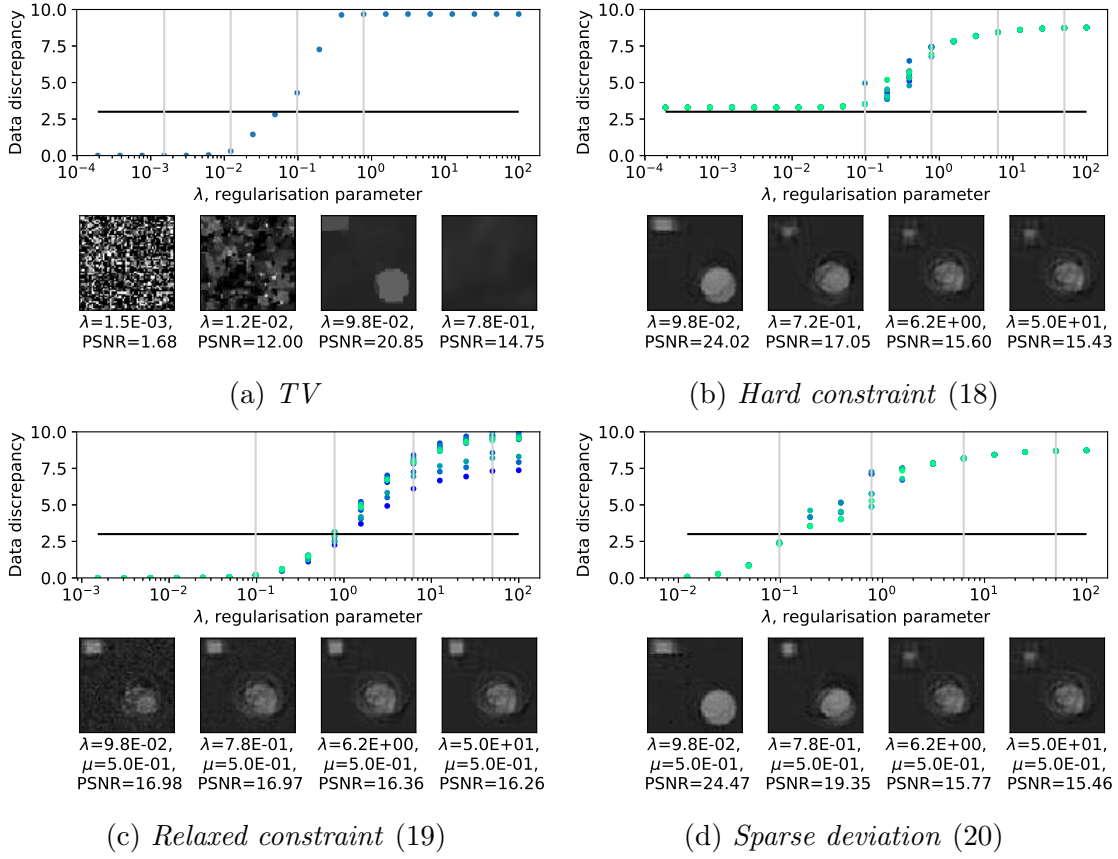


Figure 11: Solution of the inverse problem given in Figure 7(b) using a ten-dimensional AE. The plot shows the reconstruction loss against regularisation parameter choice  $\lambda$ . Where the method depends on the generator, 10 different initialisations are chosen, depicted in different colours, which are then used for each choice of regularisation parameter. The image plots correspond to the parameter values shown by the grey lines and show the best result found for given parameters.

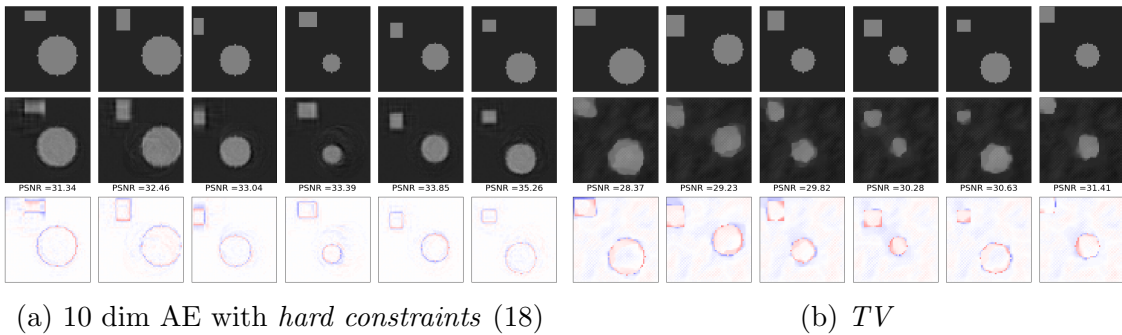


Figure 12: The worst to best reconstructions from tomography measurements on *shapes* test images. Here we compare the AE with *hard constraints* to *TV* reconstruction. The top line shows the ground truth, second line the reconstruction and bottom line the difference.

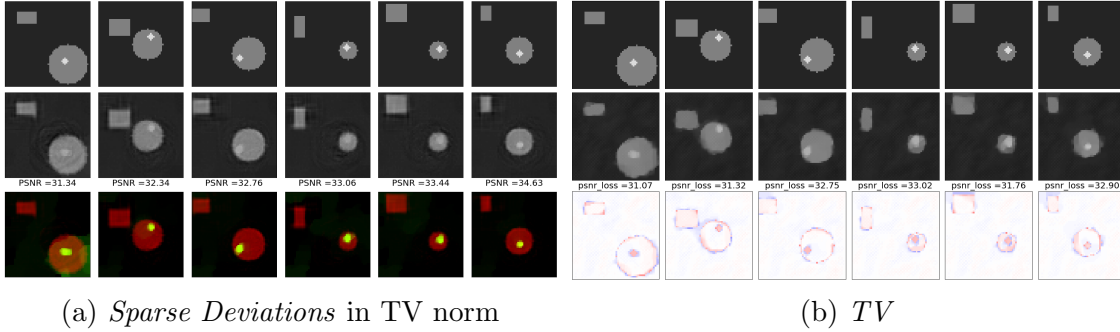


Figure 13: Tomography inverse problem (with 0.05 additive Gaussian noise) on images from the **shapes+**. On the left reconstructions use the *sparse deviation* (20) method, but with a TV norm replacing the 1-norm. The generator is a 10dim VAE trained on **shapes** images. The top line shows the ground truth, second line the reconstruction, and in the third line the part of the reconstruction lying in the range of the generator is coloured red and the sparse addition yellow ( $G(z^*)$  and  $u^*$  from (20), for red and yellow respectively). On the right the same images and inverse problem are reconstructed using TV regularisation and the top line shows the ground truth, second line the reconstruction and third line the difference.

much clearer, sharper rectangle and circle while the TV reconstruction gives shapes with unclear outlines and blob like artefacts.

In terms of computational cost, *Tikhonov* reconstruction on the tomography inverse problem on the **shapes** dataset took on average 157 iterations of backtracking until the relative difference between iteration values was less than  $10^{-8}$ . In comparison, the *hard constraint* (18) and *relaxed constraint* (19) took on average 37 and 255 iterations, respectively, without random restarts.

### 5.3. *Shapes+*

We augment the **shapes** dataset, creating the **shapes+** dataset, with the addition of a bright spot randomly located in the circle. Tomography examples (with 0.05 additive Gaussian noise) on the **shapes+** dataset are given in Figure 13. For the reconstruction we compare the *sparse deviation* reconstruction method but with the 1-norm replaced by a TV-norm ( $R_G(x) = \min_{z \in Z, u \in U} \iota_{\{0\}}(G(z) + u - x) + \|\nabla u\|_1 + \mu \|z\|_2^2$ ) with TV reconstruction. The regularisation parameters were chosen to maximise the PSNR between 20 ground truth and reconstructed images and the plots show six images spanning a range of reconstruction errors on a separate test dataset. In the *sparse deviations* case the ground truth is in the **shapes+** dataset while the VAE generator was trained on the standard **shapes** dataset. The overall reconstruction shows clear rectangles and circles and with the bright spot. The sparse deviations allow reconstruction of the bright spot without overfitting to the noise showing that generative regularisers can be effective when the ground truth images lie near, but not

in, the distribution used to train the generator. In contrast, with just  $TV$  regularisation, choosing regularisation parameters to maximise PSNR gives a solution that although finds the bright spots, loses the definition around the boundaries of the rectangles and circles. The mean PSNR for the *sparse deviation* case is 32.83 with standard deviation 0.65 and for the  $TV$  reconstruction is 32.01 with standard deviation 0.67.

#### 5.4. Knee Dataset

Examples of a tomography problems, with Gaussian noise, for the fastMRI knees dataset, are given in Figures 14 and 15. Due to the non-convex nature of the problem, 4 random restarts are taken, and the best results pictured. For the *hard constraint*, even with the random restarts on the initialisations in  $\mathcal{Z}$ , the optimisation fails to find a good reconstruction in the range of the generator. The general structure has been found, but the fine detail from the ground truth image is missing. Allowing *sparse deviations* from the range of the generator (20) gives better visual results than Tikhonov, Figures 14(a) and 15(a). The *relaxed constraint* method gives the best PSNR values.

## 6. Summary, Conclusions and Future Work

This paper looked at the use of a generator, from a generative machine learning model, as part of the regulariser of an inverse problem. We named these *generative regularisers*. Generative regularisers link the theoretically well-understood methods of variational regularisation with state-of-the-art machine learning models. The trained generator outputs data similar to training data and the regulariser restricts solutions to (close to) the range of the generator. The cost of these generative regularisers is in the generative model training, the requirement for good training data and the resulting non-convex optimisation scheme. Weighing up the costs and benefits will depend on the inverse problem and the availability of data.

We compared three different types of generative regulariser. These regularisers either restrict solutions to exactly the range of the generator or allow small deviations, measured in the 1-norm or squared 2-norm. We found that in simpler datasets, such as MNIST, if the generator was able to reconstruct images in the test set well, then reconstruction in the range of the generator was successful. Where the ground truth was more unusual, or as in one experiment, taken from a different dataset, then allowing small deviations produced the best results.

A key benefit of generative regularisers, over other deep learning approaches, is that paired training data is not required, the learning problem is unsupervised, making the method flexible to changes in the forward problem. We demonstrated the use of generative regularisers on the ill-posed inverse problems of deconvolution and fully sampled tomography, both with gradually decaying singular values of the forward operator; and compressed sensing, with a large kernel and non-unique solutions. We found that the generative models are able to provide sufficient information on the nature

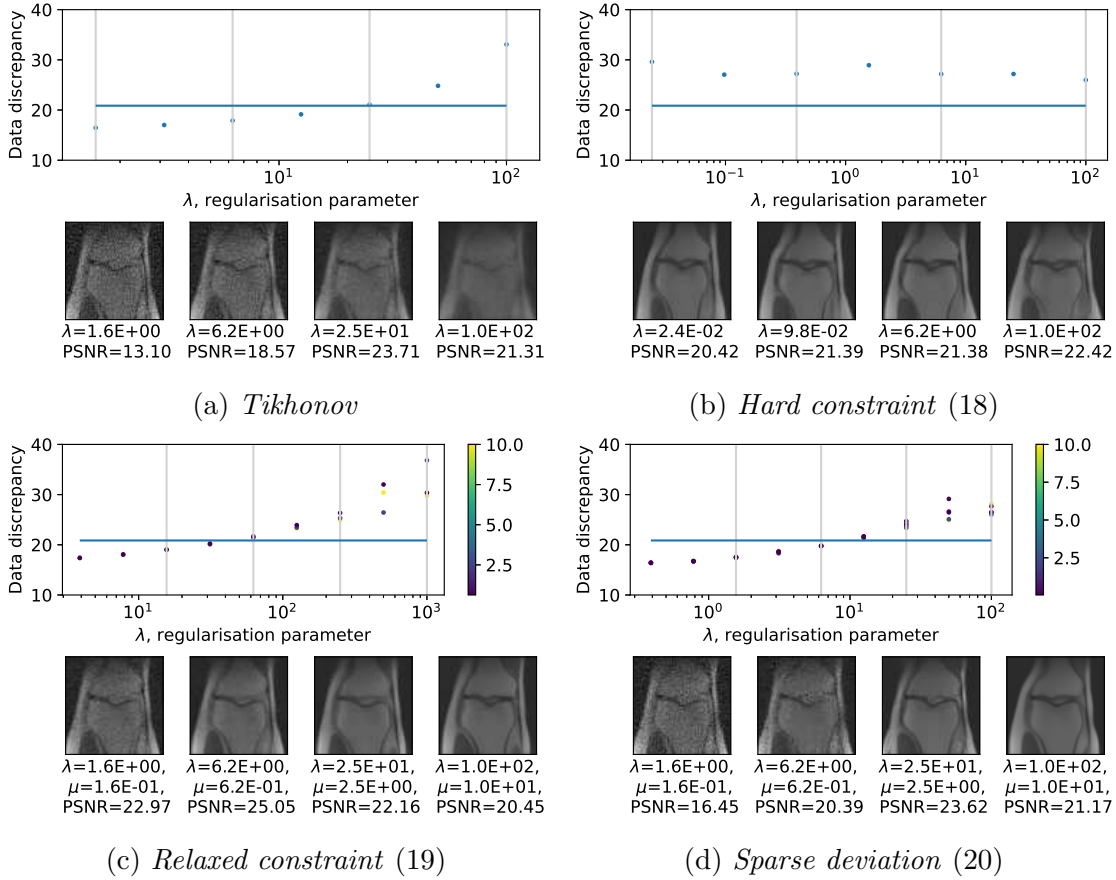


Figure 14: Solution of the inverse problem given in Figure 7(c) using an 800 dimensional VAE. The plot shows the reconstruction loss against regularisation parameter choice  $\lambda$  and, where relevant, a variety of choices for  $\mu$ , given in the colour bar. The image plots correspond to the parameter values shown by the grey lines and show the best result found for given parameters.

of solutions for compressed sensing and provide visually pleasing reconstructions for deconvolution, without instabilities. On the knee dataset, the addition of the generative model helped to combat the noise in the data.

The training of the generator is crucial to the success of generative regularisers, and a key contribution of this report is a set of desirable properties for a generator. For use in inverse problems, generated samples should be similar to samples from the training distribution and for data in the range of the generator, the corresponding point in the latent space should be recoverable. Numerical tests linked to these properties were also proposed and applied to three generative models: autoencoders (AE), variational autoencoders (VAE) and generative adversarial networks (GAN). None of these models fulfil the criteria completely. We observed known issues such as mode collapse and discriminator failure in the GAN, blurry images in the VAE and the lack of a prior in the AE. In the inverse problem experiments in this paper the AE and the VAE yielded the most consistent results. The success of the AE, despite the lack of prior on the

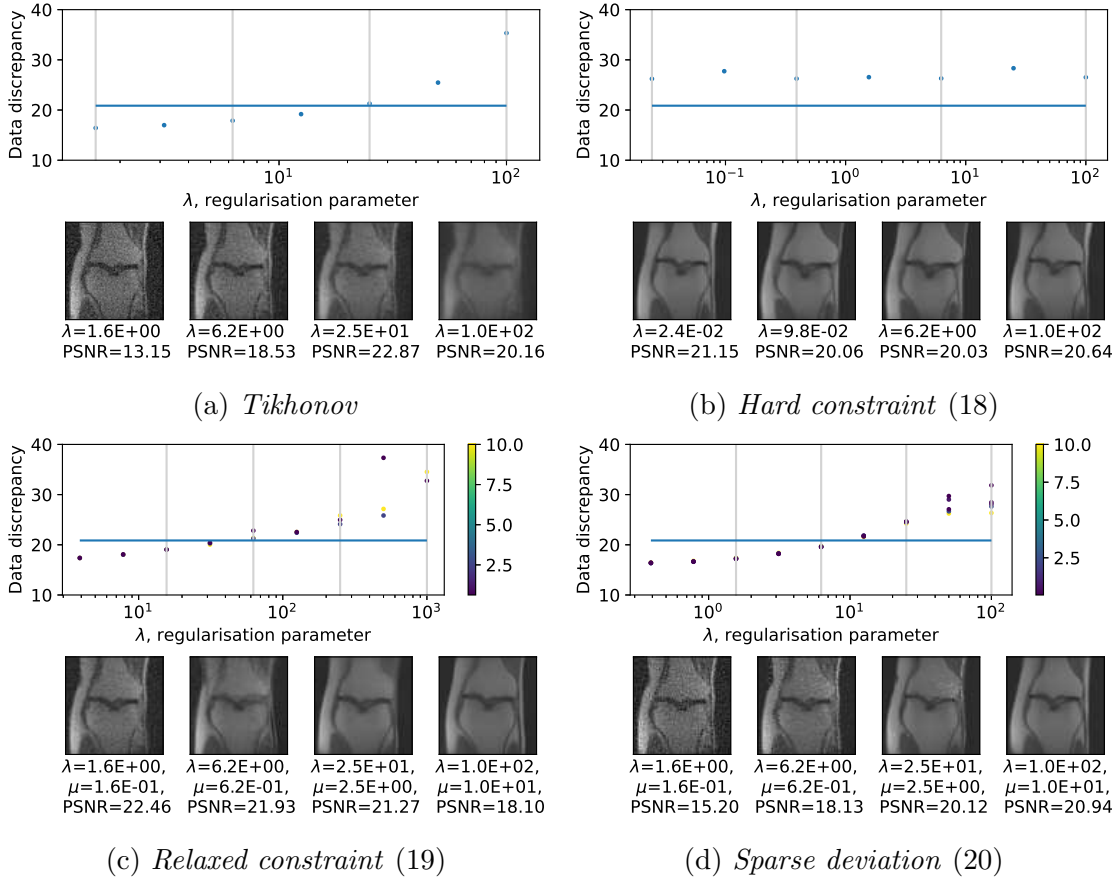


Figure 15: Solution of the inverse problem given in Figure 7(e) using an 800 dimensional VAE. The plot is laid out as in Figure 14.

latent space, surprised us. We suspect the implicit regularisation on the model from the architecture and initialisations helped make the AE a usable generator. The GAN models did worst in the inverse problem examples: they generally seemed more sensitive to initialisation of the non-convex optimisation, making the optimal point in the latent space difficult to recover. This paper did not address different initialisation strategies but future work could consider encoding a rough reconstruction in the latent space using an encoder learnt during training of the generator or separately.

This paper focused on training the generative model first and then subsequently using the generative regularisation to solve inverse problems. The benefit of this split approach is that the model does not need retraining if there are changes in the forward problem. A further advantage is that the field of generative modelling is growing quickly and any improvements to generators can be directly plugged into these methods. An interesting direction for future work would be to consider training (or refining) generative models with a particular inverse problem in mind. This is computationally more expensive but could lead to more accurate results.

## Acknowledgements

MD is supported by a scholarship from the EPSRC Centre for Doctoral Training in Statistical Applied Mathematics at Bath (SAMBa), under the project EP/L015684/1. MJE acknowledges support from the EPSRC (EP/S026045/1, EP/T026693/1), the Faraday Institution (EP/T007745/1) and the Leverhulme Trust (ECF-2019-478). NDFC acknowledges support from the EPSRC CAMERA Research Centre (EP/M023281/1 and EP/T022523/1) and the Royal Society.

**References**

- [1] Martin Abadi et al. *TensorFlow: Large-Scale Machine Learning on Heterogeneous Systems*. 2015.
- [2] R. Acar and C. R. Vogel. “Analysis of bounded variation penalty methods for ill-posed problems”. In: *Inverse Problems* 10.6 (1994), pp. 1217–1229.
- [3] Jonas Adler and Sebastian Lunz. “Banach Wasserstein GAN”. In: *NeurIPS*. Vol. 2018-Decem. 2018, pp. 6754–6763.
- [4] Jonas Adler and Ozan Öktem. “Deep Bayesian Inversion”. In: *ArXiv Preprint* (2018). arXiv: 1811.05910.
- [5] Jonas Adler et al. *Operator Discretization Library (ODL)*. 2017.
- [6] Michal Aharon et al. “K-SVD: An algorithm for designing overcomplete dictionaries for sparse representation”. In: *IEEE Transactions on Signal Processing* 54.11 (2006), pp. 4311–4322.
- [7] Giovanni S. Alberti et al. “Learning the optimal regularizer for inverse problems”. In: (2021). arXiv: 2106.06513.
- [8] Rushil Anirudh et al. “An Unsupervised Approach to Solving Inverse Problems using Generative Adversarial Networks”. In: *ArXiv Preprint* (2018). arXiv: 1805.07281.
- [9] Martin Arjovsky et al. “Wasserstein generative adversarial networks”. In: *ICML*. 2017, pp. 298–321.
- [10] Sanjeev Arora et al. “Do GANs Learn the Distribution? Some Theory and Empirics”. In: *ICLR* (2018), pp. 1–16.
- [11] Simon Arridge et al. “Solving inverse problems using data-driven models”. In: *Acta Numerica* 28 (2019), pp. 1–174.
- [12] Muhammad Asim et al. “Blind image deconvolution using pretrained generative priors”. In: *BMVC*. 2020.
- [13] Matthias Bauer and Andriy Mnih. “Resampled priors for variational autoencoders”. In: *AISTATS*. PMLR, 2018, pp. 66–75.
- [14] Martin Benning and Martin Burger. “Modern regularization methods for inverse problems”. In: *Acta Numerica* 27 (2018), pp. 1–111.
- [15] Yoeri E. Boink and Christoph Brune. “Learned SVD: solving inverse problems via hybrid autoencoding”. In: *ArXiv Preprint* (2019). arXiv: 1912.10840.
- [16] Jérôme Bolte et al. “Proximal alternating linearized minimization for nonconvex and nonsmooth problems”. In: *Mathematical Programming* 146 (2014), pp. 459–494.
- [17] Ashish Bora et al. “Compressed sensing using generative models”. In: *ICML*. 2017, pp. 822–841.
- [18] Ali Borji. “Pros and cons of GAN evaluation measures”. In: *Computer Vision and Image Understanding* 179 (2019), pp. 41–65.



- [19] Kristian Bredies and Dirk Lorenz. *Mathematical Image Processing*. Springer International Publishing, 2018.
- [20] Emmanuel J. Candes and Terence Tao. “Decoding by linear programming”. In: *IEEE Transactions on Information Theory* 51.12 (2005), pp. 4203–4215.
- [21] Antonin Chambolle and Thomas Pock. “A first-order primal-dual algorithm for convex problems with applications to imaging”. In: *Journal of mathematical imaging and vision* 40.1 (2011), pp. 120–145.
- [22] Paramanand Chandramouli et al. “Generative Models for Generic Light Field Reconstruction”. In: *TPAMI* (2020).
- [23] Xi Chen et al. “InfoGAN: Interpretable representation learning by information maximizing generative adversarial nets”. In: *NeurIPS*. 2016, pp. 2180–2188.
- [24] Donald L Cohn. *Measure theory*. Springer, 2013.
- [25] Bin Dai and David Wipf. “Diagnosing and enhancing VAE models”. In: *ICLR*. 2019.
- [26] Akshat Dave et al. “Solving Inverse Computational Imaging Problems Using Deep Pixel-Level Prior”. In: *IEEE Transactions on Computational Imaging* 5.1 (2018), pp. 37–51.
- [27] Mark A Davenport et al. *Introduction to compressed sensing*. Citeseer, 2012.
- [28] Manik Dhar et al. “Modeling Sparse Deviations for Compressed Sensing using Generative Models”. In: *ICML*. Vol. 3. 2018, pp. 1990–2005.
- [29] Sören Dittmer et al. “Regularization by Architecture: A Deep Prior Approach for Inverse Problems”. In: *Journal of Mathematical Imaging and Vision* 62.3 (2020), pp. 456–470.
- [30] Remi Flamary and Nicolas Courty. *POT Python Optimal Transport library*. 2017.
- [31] Aude Genevay et al. “GAN and VAE from an Optimal Transport Point of View”. In: *ArXiv Preprint* (2017). arXiv: 1706.01807.
- [32] Mario González et al. “Solving Inverse Problems by Joint Posterior Maximization with a VAE Prior”. In: *ArXiv Preprint* (2019). arXiv: 1911.06379.
- [33] Ian J. Goodfellow et al. “Generative adversarial nets”. In: *NeurIPS* (2014), pp. 2672–2680.
- [34] Arthur Gretton et al. “A kernel method for the two-sample-problem”. In: *NeurIPS*. 2007, pp. 513–520.
- [35] Arthur Gretton et al. “A Kernel Two-Sample Test”. In: *JMLR* 13 (2012), pp. 723–773.
- [36] Ishaan Gulrajani et al. “Improved training of wasserstein GANs”. In: *NeurIPS*. 2017, pp. 5768–5778.
- [37] Andreas Habring and Martin Holler. “A Generative Variational Model for Inverse Problems in Imaging”. In: *ArXiv Preprint* (2021). arXiv: 2104.12630.

- [38] Markus Haltmeier et al. “Sparse Lq-regularization of inverse problems with deep learning”. In: *ArXiv Preprint* (2019). arXiv: 1908.03006.
- [39] Paul Hand and Vladislav Voroninski. “Global Guarantees for Enforcing Deep Generative Priors by Empirical Risk”. In: *IEEE Transactions on Information Theory* 66.1 (2020), pp. 401–418.
- [40] Paul Hand et al. “Phase retrieval under a generative prior”. In: *NeurIPS*. 2018, pp. 9136–9146.
- [41] Chinmay Hegde. “Algorithmic Aspects of Inverse Problems Using Generative Models”. In: *56th Annual Allerton Conference on Communication, Control, and Computing*. 2019, pp. 166–172.
- [42] Martin Heusel et al. “GANs trained by a two time-scale update rule converge to a local Nash equilibrium”. In: *NeurIPS* (2017), pp. 6627–6638.
- [43] Rui Huang et al. “Beyond Face Rotation: Global and Local Perception GAN for Photorealistic and Identity Preserving Frontal View Synthesis”. In: *ICCV*. 2017, pp. 2458–2467.
- [44] Kazufumi Ito and Bangti Jin. *Inverse problems: Tikhonov theory and algorithms*. 2015.
- [45] Jörn Henrik Jacobsen et al. “I-revnet: Deep invertible networks”. In: *ICLR*. 2018.
- [46] Jean Jacod and Philip Protter. *Probability Essentials*. Springer Science & Business Media, 2004.
- [47] Maya Kabkab et al. “Task-aware compressed sensing with generative adversarial networks”. In: *AAAI*. 2018, pp. 2297–2304.
- [48] Tero Karras et al. “Progressive growing of GANs for improved quality, stability, and variation”. In: *ICLR*. 2018.
- [49] Diederik P Kingma and Prafulla Dhariwal. “Glow: Generative flow with invertible 1x1 convolutions”. In: *NeurIPS*. 2018, pp. 10215–10224.
- [50] Diederik P. Kingma and Max Welling. “Auto-encoding variational bayes”. In: *ICLR* (2014).
- [51] Florian Knoll et al. “fastMRI: A Publicly Available Raw k-Space and DICOM Dataset of Knee Images for Accelerated MR Image Reconstruction Using Machine Learning”. In: *Radiology: Artificial Intelligence* (2020).
- [52] Avisek Lahiri et al. “Faster Unsupervised Semantic Inpainting: A GAN Based Approach”. In: *ICIP*. 2019, pp. 2706–2710.
- [53] Yann LeCun et al. “Gradient-based learning applied to document recognition”. In: *Proceedings of the IEEE*. Vol. 86. 11. 1998, pp. 2278–2323.
- [54] Victor Lempitsky et al. “Deep Image Prior”. In: *CVPR*. Vol. 128. 2018, pp. 9446–9454.
- [55] Housen Li et al. “NETT: Solving inverse problems with deep neural networks”. In: *Inverse Problems* 36.6 (2020).

- [56] David Lopez-Paz and Maxime Oquab. “Revisiting classifier two-sample tests”. In: *ICLR*. 2017.
- [57] Sebastian Lunz et al. “Adversarial regularizers in inverse problems”. In: *NeurIPS*. 2018, pp. 8507–8516.
- [58] Jun Lv et al. “Which GAN? A comparative study of generative adversarial network-based fast MRI reconstruction”. In: *Philosophical Transactions of the Royal Society A* 379.2200 (2021).
- [59] Alireza Makhzani and Brendan Frey. “k-Sparse autoencoders”. In: *ICLR*. 2014.
- [60] Tim Meinhardt et al. “Learning Proximal Operators: Using Denoising Networks for Regularizing Inverse Imaging Problems”. In: *ICCV*. 2017, pp. 1799–1808.
- [61] Sachit Menon et al. “PULSE: Self-Supervised Photo Upsampling via Latent Space Exploration of Generative Models”. In: *CVPR*. 2020, pp. 2437–2445.
- [62] Lukas Mosser et al. “Stochastic Seismic Waveform Inversion Using Generative Adversarial Networks as a Geological Prior”. In: *Mathematical Geosciences* 52.1 (2020), pp. 53–79.
- [63] Dominik Narnhofer et al. “Inverse GANs for accelerated MRI reconstruction”. In: *SPIE-Intl Soc Optical Eng*, 2019, p. 45.
- [64] Frank Natterer. *The mathematics of computerized tomography*. SIAM, 2001.
- [65] Sebastian Nowozin et al. “f-GAN: Training generative neural samplers using variational divergence minimization”. In: *NeurIPS*. 2016, pp. 271–279.
- [66] Thomas Oberlin and Mathieu Verm. “Regularization via deep generative models: an analysis point of view”. In: *ArXiv Preprint* (2021). arXiv: 2101.08661.
- [67] Daniel Obmann et al. “Augmented NETT Regularization of Inverse Problems”. In: *ArXiv Preprint* (2019). arXiv: 1908.03006.
- [68] Daniel Obmann et al. “Deep synthesis regularization of inverse problems”. In: *ArXiv Preprint* (2020). arXiv: 2002.00155.
- [69] Daniel Obmann et al. “Sparse Anett for Solving Inverse Problems with Deep Learning”. In: *International Symposium on Biomedical Imaging Workshops, Proceedings*. 2020.
- [70] Daniel Obmann et al. “Sparse synthesis regularization with deep neural networks”. In: *International Conference on Sampling Theory and Applications* (2019), pp. 1–5.
- [71] Gyutaek Oh et al. “Unpaired Deep Learning for Accelerated MRI Using Optimal Transport Driven CycleGAN”. In: *IEEE Transactions on Computational Imaging* 6 (2020), pp. 1285–1296.
- [72] John Paisley et al. “Variational Bayesian inference with stochastic search”. In: *ICML*. 2012, pp. 1367–1374.
- [73] Hyoungh Suk Park et al. “Unpaired image denoising using a generative adversarial network in x-ray CT”. In: *IEEE Access* 7 (2019), pp. 110414–110425.

- [74] F Pedregosa et al. “Scikit-learn: Machine Learning in Python”. In: *JMLR* 12 (2011), pp. 2825–2830.
- [75] Pei Peng et al. “Auto-encoders for compressed sensing”. In: *NeurIPS*. 2019.
- [76] Alec Radford et al. “Unsupervised representation learning with deep convolutional generative adversarial networks”. In: *ICLR*. 2016.
- [77] Yaniv Romano et al. “The little engine that could: Regularization by Denoising (RED)”. In: *SIAM Journal on Imaging Sciences* 10.4 (2017), pp. 1804–1844.
- [78] Yossi Rubner et al. “Metric for distributions with applications to image databases”. In: *ICCV*. 1998.
- [79] Leonid I. Rudin et al. “Nonlinear total variation based noise removal algorithms”. In: *Physica D: Nonlinear Phenomena* 60.1-4 (1992), pp. 259–268.
- [80] Lars Ruthotto and Eldad Haber. “An Introduction to Deep Generative Modeling”. In: *ArXiv Preprint* (2021). arXiv: 2103.05180.
- [81] Tim Salimans et al. “Improved techniques for training GANs”. In: *Neur*. 2016, pp. 2234–2242.
- [82] Otmar Scherzer et al. “Variational regularization methods for the solution of inverse problems”. In: *Applied Mathematical Sciences (Switzerland)*. Vol. 167. Springer, 2009, pp. 53–113.
- [83] Viraj Shah and Chinmay Hegde. “Solving Linear Inverse Problems Using Gan Priors: An Algorithm with Provable Guarantees”. In: *ICASSP*. 2018, pp. 4609–4613.
- [84] Byeongsu Sim et al. “Optimal Transport Structure of CycleGAN for Unsupervised Learning for Inverse Problems”. In: *ICASSP*. 2020, pp. 8644–8647.
- [85] Jan Stanczuk et al. “Wasserstein GANs Work Because They Fail (to Approximate the Wasserstein Distance)”. In: *ArXiv Preprint* (2021). arXiv: 2103.01678.
- [86] Lucas Theis et al. “A note on the evaluation of generative models”. In: *ICLR*. 2016.
- [87] A. N. Tikhonov et al. *Numerical Methods for the Solution of Ill-Posed Problems*. 1995.
- [88] Subarna Tripathi et al. “Correction by Projection: Denoising Images with Generative Adversarial Networks”. In: *ArXiv Preprint* (2018). arXiv: 1803.04477.
- [89] Dave Van Veen et al. “Compressed Sensing with Deep Image Prior and Learned Regularization”. In: *ArXiv Preprint* (2018). arXiv: 1806.06438.
- [90] Singanallur V. Venkatakrishnan et al. “Plug-and-Play priors for model based reconstruction”. In: *GlobalSIP*. 2013, pp. 945–948.
- [91] Cédric Villani. *Optimal Transport: Old and New*. Number 338. Springer Verlag, 2009.
- [92] Yang Wang. “A Mathematical Introduction to Generative Adversarial Nets (GAN)”. In: *ArXiv Preprint* (2020). arXiv: 2009.00169.

- [93] Zhou Wang et al. “Image quality assessment: from error visibility to structural similarity”. In: *IEEE transactions on image processing* 13.4 (2004), pp. 600–612.
- [94] Tom White. “Sampling Generative Networks”. In: *ArXiv Preprint* (2016). arXiv: 1609.04468.
- [95] Shaojie Xu et al. “Fast Compressive Sensing Recovery Using Generative Models with Structured Latent Variables”. In: *ICASSP. 2019*, pp. 2967–2971.
- [96] Guang Yang et al. “DAGAN: Deep De-Aliasing Generative Adversarial Networks for Fast Compressed Sensing MRI Reconstruction”. In: *IEEE Transactions on Medical Imaging* 37.6 (2018), pp. 1310–1321.
- [97] Raymond A. Yeh et al. “Semantic image inpainting with deep generative models”. In: *CVPR. IEEE, 2017*, pp. 6882–6890.
- [98] Jure Zbontar et al. “fastMRI: An Open Dataset and Benchmarks for Accelerated MRI”. In: *ArXiv Preprint* (2018). arXiv: 1811.08839.
- [99] Jun Yan Zhu et al. “Unpaired Image-to-Image Translation Using Cycle-Consistent Adversarial Networks”. In: *ICCV. 2017*, pp. 2242–2251.

## Appendix A. Generative Model Derivations

### Appendix A.1. Mathematical preliminaries

The probabilistic approach requires some mathematical preliminaries to fully justify the derivation. For a more detailed mathematical approach see [80, 92].

Consider the image and latent spaces to be measurable spaces,  $(\mathcal{X}, \mathcal{A}_X)$  and  $(\mathcal{Z}, \mathcal{A}_Z)$ , respectively. As  $\mathcal{X}$  and  $\mathcal{Z}$  are Euclidean spaces, we choose  $\mathcal{A}_Z$  and  $\mathcal{A}_X$  to be their Borel  $\sigma$ -algebras, the smallest  $\sigma$ -algebra containing every open set [24]. We consider a *prior probability distribution on the latent space*,  $P_Z : \mathcal{A}_Z \rightarrow [0, +\infty]$  with corresponding probability density function  $p_Z$  (with respect to the Lebesgue measure). Recall the unknown *target probability distribution on the image space*  $P^* : \mathcal{A}_X \rightarrow [0, +\infty]$ . Consider a measurable (e.g. continuous) *generator*,  $G : \mathcal{Z} \rightarrow \mathcal{X}$ . Define  $G_{\#}P_Z : \mathcal{A}_X \rightarrow [0, +\infty]$  to be the *push-forward distribution* of  $G$  applied to  $P_Z$  so that for any  $B \in \mathcal{A}_X$ ,  $G_{\#}P_Z(B) := P_Z(\{z \in \mathcal{Z} | G(z) \in B\})$ . For  $f$  a real valued  $\mathcal{A}_X$ -measurable function on  $\mathcal{X}$  it holds that  $\mathbb{E}_{G_{\#}P_Z}[f] = \mathbb{E}_{P_Z}[f \circ G]$  [24, Proposition 2.6.8]. Call  $P_G := G_{\#}P_Z$  the *generated distribution*. There may not exist a corresponding density function with respect to the Lebesgue measure, as for example  $G$  may not be invertible, see for example [46, Theorem 12.7]. A random sample  $x$  from  $P_G$  can be obtained as  $x = G(z)$ , where  $z$  is a random sample from the prior  $P_Z$ .

In some modelling regimes, it may be beneficial to be able to define a continuous density distribution for  $P_G$  and so instead of the push-forward operator we use a likelihood distribution  $P(\mathcal{X} | \mathcal{Z}; G)$  which depends on the generator,  $G$ . We would then define the ‘noisy’ generated distribution  $\tilde{P}_G$  to have density

$$\tilde{p}_G(x) = \int_{\mathcal{Z}} p(x|z; G)p_z(z)dz. \tag{A.1}$$

For example, we could choose the likelihood density to be  $p(x|z; G) = \mathcal{N}(x|G_\theta(z), \rho^2 I)$  for some fixed variance  $\rho^2$  or  $p(x|z; G) = \delta(x - G(z))$ . The former could be useful when the training dataset is inherently noisy and the deviation of the training dataset from the ideal manifold can be modelled as Gaussian noise. The latter is the noiseless case and  $P_G = \tilde{P}_G$ , but again  $\tilde{p}_G(x)$  may not exist.

### Appendix A.2. Generative Adversarial Network (GAN)

The choice of Wasserstein distance in (5) leads to the Wasserstein GAN, a popular generative model [9]. Taking  $\Pi(P^*, P_G)$  to be the set of joint probability distributions with marginals  $P^*$  and  $P_G$ , the Wasserstein distance is given by

$$\mathcal{W}(P^*, P_G) = \inf_{\nu \in \Pi(P^*, P_G)} \int \|x - \tilde{x}\|_2 d\nu(x, \tilde{x}) = \inf_{\nu \in \Pi(P^*, P_G)} \mathbb{E}_{(x, \tilde{x}) \sim \nu} \|x - \tilde{x}\|_2. \quad (\text{A.2})$$

Here we have used the 2-norm as a distance measure on  $\mathcal{X}$ , but other alternatives such as  $p$ -norms or Sobolev norms are possible [3].

Equation (A.2) is intractable as, for example,  $P^*$  is unknown. We instead rewrite (A.2) using the Kantorovich–Rubinstein dual characterisation (see Remark 6.5 [91])

$$\mathcal{W}(P^*, P_G) = \sup_{D \in \text{Lip}(\mathcal{X}, \mathbb{R})} \{ \mathbb{E}_{x \sim P^*} D(x) - \mathbb{E}_{\tilde{x} \sim P_G} D(\tilde{x}) \}, \quad (\text{A.3})$$

where  $\text{Lip}(\mathcal{X}, \mathbb{R})$  denotes the space of real-valued 1-Lipschitz functions from  $\mathcal{X}$  to  $\mathbb{R}$ . For any  $D \in \text{Lip}(\mathcal{X}, \mathbb{R})$ , for almost all  $x \in \mathcal{X}$ , the gradient  $\nabla D(x)$  exists and  $\|\nabla D(x)\|_2 \leq 1$ . We call the function  $D$  a *discriminator*. The expectations can now be approximated using samples from the two distributions.

Take  $G$  and  $D$  to be parameterised functions, e.g. neural networks, with parameters  $\theta$  and  $\phi$ , respectively. Using the properties of the push-forward distribution discussed in Section Appendix A.1, the task of minimising the Wasserstein distance becomes

$$\min_{\theta} \max_{\phi} \{ \mathcal{L}(\theta, \phi) := \mathbb{E}_{x \sim P^*} D_{\phi}(x) - \mathbb{E}_{z \sim P_z} D_{\phi}(G_{\theta}(z)) \}. \quad (\text{A.4})$$

To enforce the Lipschitz constraint a penalty term,  $\mathbb{E}_{x \sim \hat{P}} (\|\nabla D_{\phi}(x)\|_2 - 1)^2$ , is added to the loss function of the discriminator. Samples of  $\hat{P}$  are calculated as  $\hat{x} = tG_{\theta}(z) + (1-t)x$  for  $t \sim \mathcal{U}[0, 1]$ ,  $x \sim P^*$  and  $z \sim P_z$  [36].

Although motivated by the Wasserstein distance, the quantity we obtain is unlikely be an accurate approximation of the Wasserstein distance [9, 31, 85]. Instead of optimising over all Lipschitz functions  $D$  in (A.2) we restricted to a family of functions parameterised by  $\phi$ . The Lipschitz constraint is also not guaranteed to hold, enforced only by the addition of the gradient penalty. Additionally, (A.2) is calculated based on finite samples not full distributions.

### Appendix A.3. Variational Autoencoder (VAE)

For another choice of distance,  $d$ , in (5), take the Kullback–Leibler (KL) divergence. This choice leads to another common generative model, the variational autoencoder (VAE) [50].

For  $P, Q$ , probability distributions on  $\mathcal{X}$ , with probability density functions  $p$  and  $q$ , where  $P$  is absolutely continuous with respect to  $Q$ , the *KL divergence from  $Q$  to  $P$*  is defined as

$$d_{\text{KL}}(P\|Q) = \mathbb{E}_{x \sim P} \log \left( \frac{p(x)}{q(x)} \right). \quad (\text{A.5})$$

Parametrising the generator,  $G$ , with values  $\theta$ , we take the KL divergence from  $\tilde{P}_{G_\theta}$  to  $P^*$ , using the ‘noisy generated’ distribution, (A.1), because of its explicit density to give

$$d_{\text{KL}}(P^*\|\tilde{P}_{G_\theta}) = \mathbb{E}_{x \sim P^*} \log \frac{p^*(x)}{\tilde{p}_{G_\theta}(x)} \quad (\text{A.6})$$

$$= \mathbb{E}_{x \sim P^*} \log p^*(x) - \mathbb{E}_{x \sim P^*} \log \tilde{p}_{G_\theta}(x). \quad (\text{A.7})$$

The first term does not depend on  $\theta$  and so minimising the KL divergence is equivalent to maximising  $\mathbb{E}_{x \sim P^*} \log \tilde{p}_{G_\theta}(x)$  with respect to the parameters  $\theta$ .

In most cases the integral for  $\tilde{p}_{G_\theta}(x)$ , defined in (A.1), is intractable. Using variational inference (note this is distinct to variational regularisation discussed in Section 1) we introduce a new density distribution on  $\mathcal{Z}$ ,  $q(\cdot; \psi)$ , from a family of functions parameterised by  $\psi$ . This distribution approximates the exact posterior on  $\mathcal{Z}$ ,  $p(\cdot|x; \theta)$ .

Starting with the definition of  $\tilde{p}_G$  in (A.1) we multiply and divide by  $q$  giving

$$\tilde{p}_{G_\theta}(x) = \int q(z; \psi) \frac{p(x|z; \theta) p_Z(z)}{q(z; \psi)} dz = \mathbb{E}_{z \sim q(\cdot; \psi)} \left[ \frac{p(x|z; \theta) p_Z(z)}{q(z; \psi)} \right]. \quad (\text{A.8})$$

Since the logarithm is concave, Jensen’s inequality results in

$$\log \tilde{p}_{G_\theta}(x) \geq \mathbb{E}_{z \sim q(\cdot; \psi)} \log \left[ \frac{p(x|z; \theta) p_Z(z)}{q(z; \psi)} \right] \quad (\text{A.9})$$

$$= \mathbb{E}_{z \sim q(\cdot; \psi)} \left[ \log p(x|z; \theta) - \log \left( \frac{q(z; \psi)}{p_Z(z)} \right) \right] \quad (\text{A.10})$$

$$= \mathbb{E}_{z \sim q(\cdot; \psi)} [\log p(x|z; \theta) - d_{\text{KL}}[q(\cdot; \psi)\|p_Z]]. \quad (\text{A.11})$$

For the KL divergence in the second term to be well defined,  $q(z; \psi)$  must vanish whenever  $p_Z(z) = 0$ , but as  $p_Z$  is usually a Gaussian distribution, this is not a concern here.

The previous calculations were standard variational inference results. We now make choices particular to the VAE. Define the prior on  $\mathcal{Z}$  to be a standard normal distribution. Introduce  $\mu_\psi, \sigma_\psi^2 : \mathcal{X} \rightarrow \mathcal{Z}$ , neural networks parameterised by  $\psi$ , and hence let  $q(\cdot; \psi)$  on  $\mathcal{Z}$  be the Gaussian distribution

$$q(\cdot|x; \psi) = \mathcal{N}(\mu_\psi(x), \text{diag}(\sigma_\psi^2(x))) := \mathcal{N}_{x, \psi}. \quad (\text{A.12})$$

In addition to the assumption that  $q$  is Gaussian, we have also made the modelling choice that the distribution depends on  $x$  through neural networks. This choice is sometimes called ‘amortised inference’. Also, let  $p(x|z; \theta)$  be normally distributed with mean  $G_\theta(z)$  and fixed variance,  $\rho^2 I$ ,

$$p(\cdot|z; \theta) = \mathcal{N}(G_\theta(z), \rho^2 I). \quad (\text{A.13})$$

Maximising the bound in (A.11) can now be written as a minimisation of

$$\mathcal{J}(\psi, \theta) = \mathbb{E}_{x \sim P^*} \left( \mathbb{E}_{z \sim \mathcal{N}_{x, \psi}} \left[ \frac{\|x - G_\theta(z)\|_2^2}{2\rho^2} \right] + d_{KL}(\mathcal{N}_{x, \psi} \| p_Z) \right) \quad (\text{A.14})$$

ignoring terms independent of  $\psi$  and  $\theta$ .

The expectation over  $P^*$  is calculated empirically using the training set but the expectation over  $\mathcal{N}_{x, \psi}$  is more complicated. In order to minimise  $\mathcal{J}$  one might want to differentiate  $\mathcal{J}$  with respect to  $\psi$ . Estimating gradients of the form  $\nabla_\psi \mathbb{E}_{z \sim \mathcal{N}_{x, \psi}} f(z)$  is possible using Monte-Carlo methods but the estimator tends to exhibit high variance [72]. A significant contribution of the original VAE paper [50], is the so called ‘reparameterisation step’. Instead consider  $z \sim \mathcal{N}_{x, \psi}$  implies  $z = \mu_\psi(x) + \epsilon \sigma_\psi(x)$  where  $\epsilon \sim \mathcal{N}(0, I)$ . Now  $\nabla_\psi \mathbb{E}_{z \sim \mathcal{N}_{x, \psi}} f(z) \approx \frac{1}{L} \sum_{i=1}^L \nabla_\psi f(\mu_\psi(x) + \epsilon^{(i)} \sigma_\psi)$  where  $\epsilon^{(i)} \sim \mathcal{N}(0, I)$ . This approximation is experimentally seen to be more stable and values as small as  $L = 1$  are regularly used.

## Appendix B. Generative Model Architectures

The architectures for the three different generative models, for the different datasets are given in this Appendix.

<p><b>Down-conv:</b> <math>[f_1, f_2, \dots, f_l]</math>,  <math>[s_1, s_2, \dots, s_l]</math>, <math>[k_1, k_2, \dots, k_l]</math>,  activation,  <math>[d_1, d_2, d_3]</math></p>	<p>Convolution with <math>f_1</math> filters, <math>k_1 \times k_1</math> kernel, stride <math>s_1</math>, activation  Dropout layer (prob=0.8)  :  Convolution with <math>f_l</math> filters, <math>k_l \times k_l</math> kernel, stride <math>s_l</math>, activation  Dropout layer (prob=0.8)  Output size=<math>[d_1, d_2, d_3]</math></p>
<p><b>Up-conv:</b> <math>[f_1, f_2, \dots, f_l]</math>,  <math>[s_1, s_2, \dots, s_l]</math>, <math>[k_1, k_2, \dots, k_l]</math>,  activation,  <math>[d_1, d_2, d_3]</math></p>	<p>Convolution transpose with <math>f_1</math> filters, <math>k_1 \times k_1</math> kernel, stride <math>s_1</math>, activation  Dropout layer (prob=0.8)  :  Convolution transpose with <math>f_l</math> filters, <math>k_l \times k_l</math> kernel, stride <math>s_l</math>, activation  Dropout layer (prob=0.8)  Output size=<math>[d_1, d_2, d_3]</math></p>

Figure B1: Definitions used in Figure B2, B3 and B4.



Encoder/Discriminator			Decoder/Generator		
AE	VAE	GAN	AE	VAE	GAN
Input shape = $[n, n, 1]$			Input shape = [latent dimension]		
<b>Down-conv:</b> $[64, 64, 64], [2, 2, 1], [4, 4, 4], \text{LeakyReLU}, [\frac{n}{4}, \frac{n}{4}, 64]$			Dense layer, LeakyReLU, $[\frac{n^2}{16}]$ Dense layer, LeakyReLU, $[\frac{n^2}{16}]$ Reshape, $[\frac{n}{4}, \frac{n}{4}, 1]$		
Reshape, $[16n^2]$			<b>Up-conv:</b> $[64, 64, 64], [1, 2, 2], [4, 4, 4], \text{ReLU}, [n, n, 64]$		
Dense layer, [latent dimension]	Dense layer, $[2*\text{latent dimension}]$	Dense layer, [1]	Reshape, $[64n^2]$		
			Dense layer, $[n^2]$ Reshape, $[n, n]$		

Figure B2: The architectures for the 3 generative models, AE, VAE and GAN, for the MNIST dataset. The convolution block definitions are given in Figure B1.

Encoder/Discriminator			Decoder/Generator		
AE	VAE	GAN	AE	VAE	GAN
Input shape = $[n, n, 1]$			Input shape = [latent dimension]		
<b>Down-conv:</b> $[64, 64, 64], [1, 2, 2], [4, 4, 4], \text{LeakyReLU}, [\frac{n}{4}, \frac{n}{4}, 64]$			Dense layer, LeakyReLU, $[\frac{n^2}{64}]$ Reshape, $[\frac{n}{8}, \frac{n}{8}, 1]$		
Reshape, $[16n^2]$			<b>Up-conv:</b> $[64, 64, 64], [2, 2, 1], [4, 4, 4], \text{LeakyReLU}, [n, n, 64]$		
Dense layer, [latent dimension]	Dense layer, $[2*\text{latent dimension}]$	Dense layer, [1]	Reshape, $[64n^2]$		
			Dense layer, $[n^2]$ Reshape, $[n, n]$		

Figure B3: The architectures for the 3 generative models, AE, VAE and GAN, for the shapes dataset. The convolution block definitions are given in Figure B1.

Encoder/Discriminator	Decoder/Generator
VAE	VAE
Input shape = $[n, n, 1]$	Input shape = [latent dimension]
	Dense layer, ReLU, $[\frac{n^2}{8}]$ Reshape, $[\frac{n}{16}, \frac{n}{16}, 16]$
<b>Down-conv:</b> [8,16,32], [1, 1, 1], [3, 3, 3], LeakyReLU, $[n, n, 32]$ <b>Down-conv:</b> [64, 64, 64], [2, 1, 1], [3, 3, 3], LeakyReLU, $[\frac{n}{2}, \frac{n}{2}, 64]$ <b>Down-conv:</b> [128, 128, 128], [2, 1, 1], [3, 3, 3], LeakyReLU, $[\frac{n}{4}, \frac{n}{4}, 128]$ <b>Down-conv:</b> [256, 256, 256], [2, 1, 1], [3, 3, 3], LeakyReLU, $[\frac{n}{8}, \frac{n}{8}, 256]$ <b>Down-conv:</b> [64, 32, 8], [1, 1, 1], [3, 3, 3], LeakyReLU, $[\frac{n}{8}, \frac{n}{8}, 8]$	<b>Up-conv:</b> [32, 64, 128, 256], [1, 1, 1, 1], [3, 3, 3, 3], ReLU, $[\frac{n}{16}, \frac{n}{16}, 256]$ <b>Up-conv:</b> [512, 512, 512, 512], [1, 1, 1, 1], [3, 3, 3, 3], ReLU, $[\frac{n}{16}, \frac{n}{16}, 512]$ <b>Up-conv:</b> [256, 256, 256, 256], [2, 1, 1, 1], [3, 3, 3, 3], ReLU, $[\frac{n}{8}, \frac{n}{8}, 256]$ <b>Up-conv:</b> [128, 128, 128, 128], [2, 1, 1, 1], [3, 3, 3, 3], ReLU, $[\frac{n}{4}, \frac{n}{4}, 128]$ <b>Up-conv:</b> [64, 64, 64, 64], [2, 1, 1, 1], [3, 3, 3, 3], ReLU, $[\frac{n}{2}, \frac{n}{2}, 64]$ <b>Up-conv:</b> [32, 16, 8, 4], [2, 1, 1, 1], [3, 3, 3, 3], ReLU, $[n, n, 8]$
Dense layer, $[2 * \text{latent dimension}]$	<b>Up-conv:</b> [1], [1], [3], ReLU, $[n, n, 1]$

Figure B4: The architectures for the knee dataset VAE. The convolution block definitions are given in Figure B1.